Università degli Studi Roma Tre

DIPARTIMENTO DI MATEMATICA E FISICA
Dottorato di Ricerca in Fisica

XXVI Ciclo

Active Dynamics in a Bacterial Bath

Ph.D. Candidate
Alessia Lepore

Tutors
Dr. Roberto Di Leonardo

Prof. Antonio Di Carlo

Ph.D. Coordinator
Prof. Roberto Raimondi

Anno Accademico 2012-2013

General introduction

Active matter is one of the novel and most fascinating topics in soft matter physics. This term describes a huge class of systems spanning from microscopic to macroscopic scale. These systems can be modeled in terms of single units or as a collection of such individual units moving by taking energy from internal source or from their environment. These self-propelled or active units such as motile microorganisms, Janus particles or starlings and fishes display complex dynamics far from thermal equilibrium.

In particular, motile microorganisms have developed interesting swimming strategies to overcome the limitations imposed by the low Reynolds number due to their small size [1]. In an environment where viscous forces dominate over inertial forces, microorganisms such as the algae *Chlamydomonas reinhardtii* or the bacterium *Escherichia coli* move beating flexible oars or rotating a corkscrew-like helical bundle. Both kind of these organisms use flagella to move: in *Chlamydomonas* flagella form flexible oars, while in *E.coli* they form a helical bundle. Describing and understanding the dynamics of these biological systems is an attractive challenge for experimental and theoretical physics. In *E.coli*, the flagellar motors push the cell forward for a certain persistence length, interrupted by a sudden change in direction, which produces a the characteristic run-and-tumble motion [2]. This dynamics, while diffusive at large temporal and spatial scales, can be considered as ballistic at small time and space scales. Most importantly, this process needs metabolic energy or a food source to be realized, which characterizes systems far form thermal equilibrium [3]. Therefore, run-and-tumble motion represents a good paradigm to describe an out-of-equilibrium dynamics.

A first investigation can be done on the effects of the application of an external

field on bacteria suspensions [4]. The sedimentation effect on non-motile colloidal particles is well known: it results in a stationary density profile which depends on the drift velocity in gravitational field and a diffusion coefficient, according to the Boltzmann law. Bacteria move with a certain run speed and a statistically given tumbling rate. Consequently, a steady state is reached, the stationary density profile depends on an effective diffusion coefficient related to bacteria speed and tumbling rate. Recently, the sedimentation effect in active matter has been investigated using Janus particles [5]. These particles, as suggested by their name, are composed of two halves having different chemical properties. They self-propel in presence of hydroxyl peroxide fuel. In a gravitational field, Janus particles display a steady density profile conforming with the Boltzmann law with an effective diffusion coefficient. Since the effective diffusion coefficient can be thought as resulting from an effective temperature, active systems may be said to be "hot" colloids.

The rectification effect is another intriguing aspect of run-and-tumble dynamics. A bacterium approaching a straight wall aligns its motion, continuing to swim in the same direction even after the wall end, until the next tumbling event. Thus, bacteria near a wall rectify their motion. This effect has been used to concentrate bacteria on one side of a two-dimensional bipartite micro-device, having at its center a wall made of asymmetric funnel-shaped barriers. The funnel shape makes the probability of crossing the barrier asymmetric, leading to different stationary states in bacteria density distributions over the two sides [6]. Furthermore, bacteria can rectify their motion in asymmetric environments and cooperatively work. In fact, it has been observed that in an active bacterial bath, an asymmetric micro-cog rotates unidirectionally [7].

In this thesis, both aspects related to run-and-tumble motion are inquired. In particular, we apply a centrifugal field to study the space-dependent motility distribution and to test the centrifugation method to separate cells according to their motility [8], whereas, in order to study bacteria suspensions in asymmetric landscapes, we build a three dimensional structure where passive colloidal particles can be spatially organized by a suspension of swimming bacteria [9]. To characterize our *E.coli* samples and to choose the best growth protocol [10], we use Image Correlation Spectroscopy (ICS). This imaging technique, based on the Fourier analysis, permits a fast and accurate analysis of the sample and allows us to characterize the dynam-

ical parameters of the cells. We have used the ICS technique also for studying the effects of centrifugal forces on bacteria suspensions [11]. More recently, we started to investigate the interaction between individual bacteria using the holographic optical twezeers [12, 13]. We are also testing a fluorescent labeling protocol (described in [14]), make to observable the whole cell, including its minute flagellar filaments. Our experiments are designed and performed aiming at improving our understanding of active system and at opening new technological perspectives.

Contents

Chapter 1

Active suspensions of swimming bacteria

Active matter is a term which describes a material (either in the continuum or naturally decomposable into discrete units), which is driven out of equilibrium through the transduction of energy derived from an internal energy depot or ambient medium into work performed on the environment. G.I. Menon[15]

1.1 Introduction

Active suspensions of swimming bacteria are comprised by self-propelled units, independent of each other but able to interact, and thus exhibiting a collective behavior. These units move using energy sources from the environment for instance, in presence of a chemical gradient, bacteria perform chemotaxis, directing themselves towards or against the gradient [16]. Bacteria, whose typical size is of the order of few microns, have developed swimming strategies different from those adopted by larger organisms. As explained in Sec.1.2, microscopic swimmers experience viscous forces that overshadow inertial forces.

Bacteria dynamics as the dynamics of all living matter is intrinsically out of thermal equilibrium. Describing and understanding these systems is an interesting challenge for theoretical and experimental physics. In particular "run-and-tumble" dynamics, as described in Sec.1.3, is a nice out-of-equilibrium paradigm. Also the study of

bacterial suspension under an external field such as gravity provide sample of non-equilibrium steady states. Sec.1.4 introduces a model to describe the effects of an external field on bacteria suspensions. In Sec.1.5 a sedimentation experiment is reported, where it is shown that active colloids may rightly be considered as "hot" colloids. Finally, Sec.1.6 illustrates how bacteria in an asymmetric environment such as a funnels or a ratchet rectify their motion.

1.2 Swimming at low Reynolds number

A swimmer of linear size ℓ moving with speed v in an (incompressible, linearly viscous) fluid of density ρ and viscosity η, experiences different forces according to its dimension. Indeed, defining the Reynolds number Re as the ratio between inertial and viscous forces [1] and assuming that the typical velocity scales linearly whit the size ($v = \ell/t_0$ with t_0 independent of ℓ), one has that Re depends on the square of the swimmer's size:

$$\mathrm{Re} = \frac{\ell v \rho}{\eta} = \frac{a^2 \rho}{\eta t} \tag{1.1}$$

In water $\rho \approx 10^3 \mathrm{Kg\ m^{-3}}$, $\eta \approx 10^{-3} \mathrm{Pa\ s^{-1}}$, for bacteria with speed around $10 - 20\ \mu\mathrm{m\ s^{-1}}$, $\mathrm{Re} \approx 10^{-4} - 10^{-5}$; for a small fish Re is about 10^2 and for a man swimming in water $\mathrm{Re} \approx 10^4 - 10^5$ [1, 17]. Therefore, in the microscopic world of bacteria, viscous forces dominate over inertial forces and Navier-Stokes equations at low Reynolds number reduce to the Stokes equations:

$$\begin{cases} -\nabla p + \eta \Delta \mathbf{u} = 0 \\ \mathrm{div}\, \mathbf{u} = 0 \end{cases} \tag{1.2}$$

where p is the pressure and $\mathbf{u}$ the velocity of the surrounding fluid. Equations (1.2) are linear and time-independent, so time is irrelevant and it is crucial for a swimming microorganism to deform by cyclic non-reciprocal motion. The so-called scallop theorem [1] clarifies this point: a scallop has only one degree of freedom in configuration space and can move just doing a reciprocal motion. If the scallop lived

in the microscopic world of bacteria, it would only be able to wobble back and forth around its initial position (Fig.1.1).

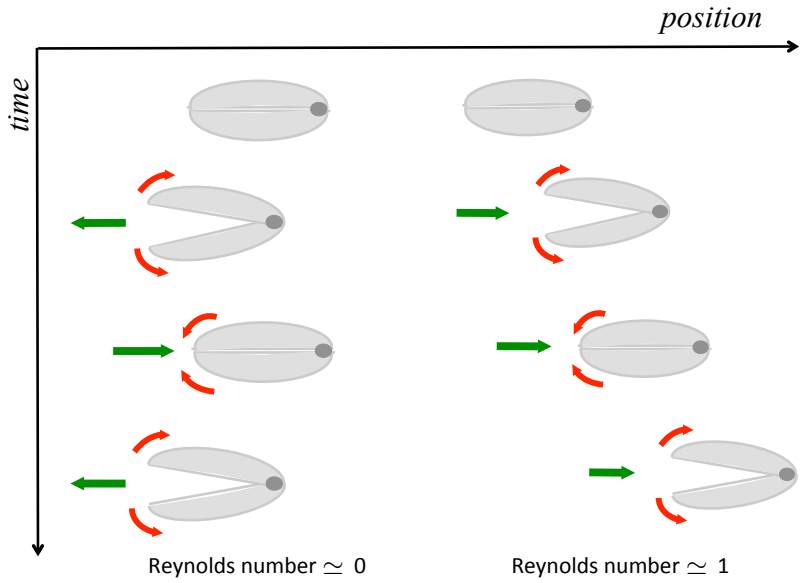

Figure 1.1: Schematic representation of the scallop motion at zero Reynolds number (left) and in its actual motion conditions (right). Re $\simeq 1$ for a scallop of $\sim$ 2cm. The green arrows represent the direction of motion.

In fact, microorganisms have developed geometric configurations like flexible oar and corkscrew to swim at low Reynolds number (Figs. 1.2, 1.3). A negligible Reynolds number implies also an instantaneous response of the surrounding fluid to the shape changes. Since inertia force is negligible, force and torque balances take form

$$\mathbf{F}_{ext}(t) + \mathbf{F}(t) = 0 \tag{1.3}$$

$$\mathbf{L}_{ext}(t) + \mathbf{L}(t) = 0 \tag{1.4}$$

where $\mathbf{F}_{ext}$ and $\mathbf{L}_{ext}$ are the external force and torque due to external fields (such as gravity), $\mathbf{F}$ and $\mathbf{L}$ are force and torque exerted on the swimmer by the fluid [17].

The motion of a rigid body in a viscous fluid is parameterized by its centre-of-mass velocity $\mathbf{U}$ and the set of angular velocities $\mathbf{\Omega}$. On its surface the velocity is $\mathbf{v} = \mathbf{U} + \mathbf{\Omega} \times \mathbf{r}$.

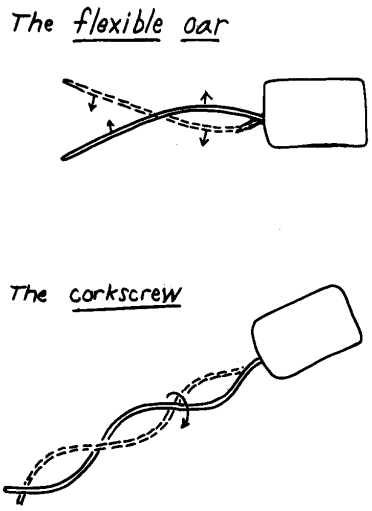

Figure 1.2: A cartoon of possible geometric configurations for propulsion at low Reynolds number. Purcell drew these figures for a talk transcribed into his famous paper *"Life at low Reynolds number"* [1].

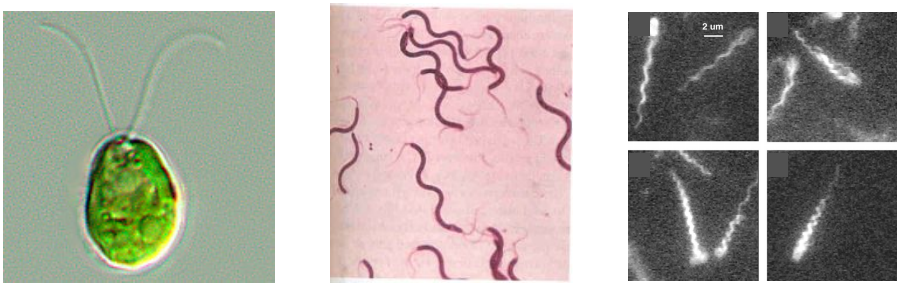

(a) *Chlamydomonas reinhardtii* (b) *Spirillum volutans* (c) *Escherichia coli*

Figure 1.3: Different swimming strategies at low Reynolds number: (a) *Chlamydomonas reinhardtii* moves beating its flexible oar (from https://wiki.umn.edu); (b) *Spirillum volutans* moves spinning its body and its tails (from http://www.cram.com/); (c) *Escherichia coli* swims rotating its flagellar bundle like a corkscrew (image reproduced from [14]).

The linearity of Stokes' equation leads to a linear relation between $(\mathbf{F}, \mathbf{T})$ and $(\mathbf{U}, \mathbf{\Omega})$:

$$\begin{pmatrix} \mathbf{F} \\ \mathbf{T} \end{pmatrix} = \begin{pmatrix} \mathbf{A} & \mathbf{B} \\ \mathbf{C} & \mathbf{D} \end{pmatrix} \begin{pmatrix} \mathbf{U} \\ \mathbf{\Omega} \end{pmatrix} \tag{1.5}$$

The matrix in Eq.(1.5) is called resistance matrix of the body. The matrix elements depend on the surrounding fluid viscosity and on the shape and size of the swimmer. In the absence of hydrodynamic interactions the matrix is symmetric and $\mathbf{B} = \mathbf{C}$ [18]. Its elements dimensionally scale as : $[\mathbf{A}] \sim \eta L$, $[\mathbf{B}] \sim \eta L^2$, $[\mathbf{D}] \sim \eta L^3$, where L is the typical length scale [17]. The swimmers shows in Figs.1.2, 1.3 can be modeled as composed by two hydrodynamically independent units linked together. In a particular case such as *Escherichia coli* (see Fig.1.3(c)), the two units are the body and the flagellar bundle [22, 26]. The flagellar bundle is modeled as a rigid helix rotating around its axis [18]. The resistance matrixes for the body and the flagella are respectively:

$$R_b = \begin{pmatrix} \mathbf{A}_b & 0 \\ 0 & \mathbf{C}_b \end{pmatrix}, \tag{1.6}$$

$$R_f = \begin{pmatrix} \mathbf{A}_f & \mathbf{B}_f \\ \mathbf{B}_f^T & \mathbf{C}_f \end{pmatrix}. \tag{1.7}$$

In the body resistance matrix (1.6) the coupling off-diagonal terms are null because the body is not self-propelling (see Chapter 2). Using eqs. (1.6), (1.7) and follow-

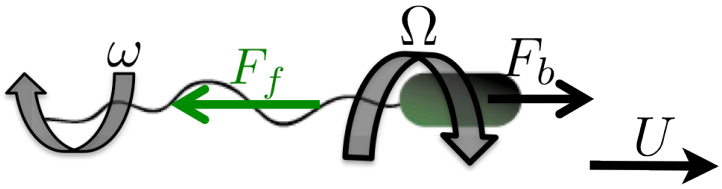

Figure 1.4: Schematic representation of force and torque acting on *E.coli*: the whole bacterium swims with speed U, the cell body rotates with angular velocity Ω, while the flagellar bundle rotates in the opposite direction with angular velocity ω. Also forces acting on the body and the flagella (F_b and F_f, respectively) are applied in opposite directions.

ing the representation in Fig.(2.2), the total force and torque acting on the whole bacterium, are:

$$F_{tot} = F_b - F_f = (A_f - A_b)\, U + B_f \omega \tag{1.8}$$

$$T_{tot} = T_b - T_f = -B_f U + C_b \Omega - C_f \omega \tag{1.9}$$

1.3 Run-and-tumble as a paradigm of non equilibrium dynamics

Run-and-tumble dynamics is characterized by straight swimming lines, named "runs", interrupted by sudden random changes of direction, named "tumbles", occurring with a rate λ (Fig 1.5). The typical run time τ_r is about 1s, while the tumble duration τ_t is about 0.1s. The run speed and tumble rate depend on environmental conditions and can vary in space. Furthermore, at time and spatial scale larger than $1/\lambda$ and v/λ, run-and-tumble dynamics can be considered as a random walk with a diffusive coefficient $v^2/\lambda d$, where d is the space scale. The run-and-tumble motion in bacteria, needing a metabolic energy source constitutes an out-of-equilibrium process [3]. Hence, run-and-tumble dynamics is far form thermal equilibrium, but still diffusive at large enough scales. These features make the run-and-tumble motion a good paradigm for the study of non-equilibrium dynamics.

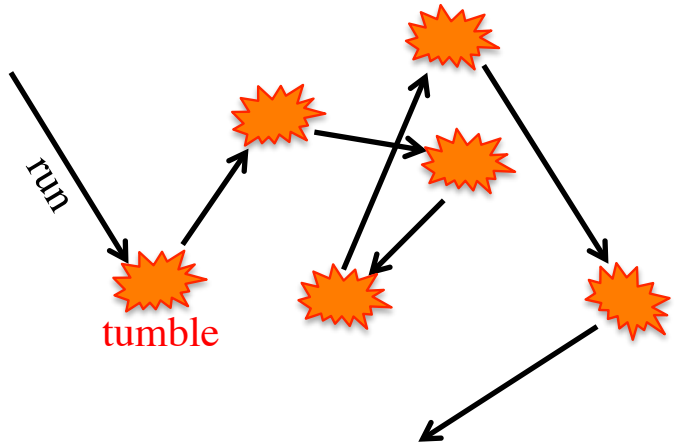

Figure 1.5: Schematic representation of run and tumble motion.

1.3.1 One-dimensional dynamics

In the one-dimensional case, a run-and-tumble particle can just move straight in one direction or in the other one. We shall describe it as a particle moving on a line with speed v (we consider a general case where $v = v(x)$) and rate $\lambda/2$ of switching direction (we assume that switching from the left to right and from right to left are equiprobable). Following Refs.[19, 20] we enforce the conservation of number of particles moving right or left :

$$\partial_t R = -\partial_x(vR) + \frac{\lambda}{2}(L - R) \tag{1.10}$$

$$\partial_t L = \partial_x(vL) + \frac{\lambda}{2}(R - L) \tag{1.11}$$

where R (L) is the density of right (left) moving particles. The total density of bacteria is $\rho = L + R$ and the flux of the particles is $J = v(R - L) = v\sigma$. Adding and subtracting Eqs.(1.10) and (1.11) yields:

$$\partial_t \rho = -\partial_x(v\sigma) = -\partial_x J \tag{1.12}$$

$$\partial_t \sigma = -\partial_x(v\rho) - \lambda\sigma \tag{1.13}$$

To study the diffusive process the second time derivative of ρ is computed from Eq.(1.12) and combined with Eq.(1.13) gives:

$$\partial_t^2 \rho = \partial_x[v\,\partial_x(v\rho)] + \lambda\partial_x J \tag{1.14}$$

Consider a system of particles moving over an interval of L. The process becomes diffusive at $t \gg \lambda L^2/v^2$, after the particles have explored all the interval and the number of particles rightward-bound and leftward-bound is the same. The flux J is null and the equilibrium configuration is reached. To study the diffusive behavior the second time derivative of ρ is to be neglected, which involves a loss of information only on the ballistic motion over short time intervals of the order $\Delta t \gg 1/\lambda$. Integrating Eq.(1.14), the flux of particles is:

$$J = -\frac{v^2}{\lambda}\partial_x\rho - \frac{v\rho}{\lambda}\partial_x v \tag{1.15}$$

where constant terms are ignored. In Eq.(1.15), the term depending on $\partial_x\rho$ is the contribution due to diffusion, while the second term account for the drift velocity $v_d = \frac{v}{\lambda}\partial_x v$. The expression (1.15) of particles flux depends on the properties of the parameters v and λ. The simple case, with λ and v both constant, gives the Eq.(1.15) in the Fick's form:

$$J = -D\partial_x\rho \tag{1.16}$$

with a diffusion coefficient $D = v^2/\lambda$.

From v constant and λ as function of the position $D = D(x)$, the equilibrium solution is a uniform particle density, $\rho = \rho_0$. In fact, changing the tumbling rate λ only affects the rate at which equilibrium is reached.

If v and λ both depend on space, but their ratio is constant, Eq.(1.15) becomes:

$$J = -\partial_x\left(D\rho\right) \tag{1.17}$$

The equilibrium density is:

$$\rho = \rho_0\left(\frac{D_0}{D}\right) = \rho_0\left(\frac{v_0^2\lambda}{v^2\lambda_0}\right) = \rho_0\left(\frac{v_0^2}{v^2}\right) \tag{1.18}$$

where ρ_0 and D_0 are, respectively, the density and diffusion coefficient taken in a reference place x_0 where the speed is v_0.

In the case in which λ is constant but v is not, one has:

$$J = -D\partial_x\rho - \frac{\rho}{2}\partial_x D \tag{1.19}$$

Then, the solution at equilibrium is given by:

$$\rho = \rho_0\left(\frac{D_0}{D}\right)^{1/2} = \rho_0\left(\frac{v_0}{v}\right) \tag{1.20}$$

The Eqs.(1.18) and (1.20) point out that the equilibrium density of run-and-tumble particles in one-dimension is inversely proportional to the particles speed but independent of the tumbling rate (for a instantaneous tumble). This result implies that bacteria will accumulate in places where they are slower.

1.3.2 Three-dimensional dynamics

In 3D, let $P(\mathbf{r}, \mathbf{v}, t)$ the density of particle at $\mathbf{r}$ at time t moving in the direction of $\mathbf{v} = v\hat{\mathbf{u}}$ where v is the speed of particles and $\hat{\mathbf{u}}$ is a unit vector. The direction of motion can vary in solid angle Ω, verifying $\Omega = \int d\ \hat{\mathbf{u}}'$. Analogously to §1.3.1, the density ρ and the flux $\mathbf{J}$ of particles are:

$$\begin{aligned} \rho(\mathbf{r}, \mathbf{v}, t) &:= \int P(\mathbf{r}, v_0\hat{\mathbf{u}}', t) d\ \hat{\mathbf{u}}' \\ \mathbf{v}\sigma(\mathbf{r}, t) \equiv \mathbf{J}(\mathbf{r}, t) &:= v_0 \int P(\mathbf{r}, v_0\hat{\mathbf{u}}', t)\hat{\mathbf{u}}' d\ \hat{\mathbf{u}}' \end{aligned} \tag{1.21}$$

Hence,

$$\begin{aligned} \partial_t P &= -\mathbf{v}\partial_{\mathbf{r}} P - \lambda P + \frac{\lambda}{\Omega} \int P(\mathbf{r}, v_0\hat{\mathbf{u}}', t) d\ u' \\ &= -\mathbf{v}\partial_{\mathbf{r}} P - \lambda P + \frac{\lambda\rho}{\Omega} \end{aligned} \tag{1.22}$$

The equilibrium solution of Eq.(1.22) is:

$$\rho = \rho_0 \tag{1.23}$$

$$P = \frac{\rho_0}{\Omega} \tag{1.24}$$

the equilibrium density ρ_0 is the total number of particles divided by the volume of space, i.e. $\rho_0 = N/V$. Choosing a particles gradient $\nabla\rho$ constant over a time and space, it is found an other steady-state solution of (1.22):

$$P = \frac{\rho}{\Omega} - \frac{\mathbf{v}\nabla\rho}{\lambda\Omega} \tag{1.25}$$

The particles flux arising from Eq.(1.25) is:

$$\mathbf{J} = -\frac{v^2}{3\lambda}\nabla\rho \tag{1.26}$$

Therefore, the 3D flux of a system of run-and-tumble particles is still in the form of Fick's law with a diffusion coefficient $D = v^2/3\lambda$.

1.4 Active matter in an external field

As a preliminary to the study of the action of an external field on bacterial suspensions, it is convenient to describe the simpler action of an external field on passive colloids.

A colloidal particle, subject to an external force $\mathbf{F}$, moves with mean velocity $\mathbf{v} = \mu\mathbf{F}$ where μ is the mobility. If $\mathbf{F}$ is conservative, the equilibrium density distribution is Boltzmannian:

$$\rho(r) \propto \exp\left[-\frac{U(r)}{k_B T}\right] \tag{1.27}$$

where $U(r)$ is the potential energy such that $\mathbf{F} = -\nabla U$ and k_B is the Boltzmann constant.

If the external field is constant such as gravity a colloidal suspension, initially uniformly distributed, at equilibrium exhibits a non uniform density distribution along the direction of external field. As Perrin showed in his famous experiment [21], each particle experiences a force defined by:

$$F_g = -\frac{4}{3}\pi a^3 \left(\rho_c - \rho_{H_2O}\right) g \tag{1.28}$$

where a is the radius of the spherical particle, the term $\left(\rho_c - \rho_{H_2O}\right) g$ is the buoyant force and g is the gravitational acceleration.

Considering $U(z) = F_g z$ the potential energy, the particles density is:

$$\rho(z) = \rho_0 \exp\left(-\frac{F_g z}{k_B T}\right) = \rho_0 \exp\left(-\frac{z}{z_0}\right) \tag{1.29}$$

where $z_0 = k_B T / F_g$ is the sedimentation length. Using the Einstein relation $D = \mu k_B T$:

$$\rho(z) = \rho_0 \exp\left(-\frac{\mu U(z)}{D}\right) \tag{1.30}$$

Since, a bacterial suspension is far from thermal equilibrium, the Einstein relation is not valid for describing these self-propelled particles. Tailleur and Cates [4] have presented some analytic results for a model of run-and-tumble bacteria under an external field. They have derived an expression for the steady state probability

density $P(z)$ to observe a bacterium at height z. They start by assuming that the swimmer either moves upwards, $c = 1$, or downwards, $c = -1$. The model is defined by:

$$P(z)dz = \sum_{c=\pm 1} P(c, z)dz \tag{1.31}$$

$$P(c, z)dz = \frac{\lambda}{2} \int_0^\infty P(z_i(z, c, \tau))dz_i e^{-\lambda\tau} d\tau \tag{1.32}$$

$P(c, z)$ is the probability of finding bacteria at the height z in the state c. Eq.(1.32) involves the probability of tumbling in the selected time interval, the probability of finding a bacterium at a height such that it could reach the height z and the probability that another tumble event occurs in the meanwhile. Eq.(1.32) considers that a tumble occurs between z_i and $z_i + dz_i$ in a time interval $(\tau, \tau + d\tau)$. The swimmer experiences a force $F_g = -\Delta mg$ in position $z_i = z - (v_c - v_d)\tau$ where v_c is the velocity of bacteria in c-state and $v_d = -\mu F_g$ is the drift speed. The sum (1.32) over c states gives the expression of $P(z)dz$.
The expression of $P(z)$ is found in [4] via Fourier transform.
Defining $\tilde{P}(\omega) = \int_{-\infty}^{\infty} P(z)exp(-i\omega z)dz$, for 1.31 and 1.32:

$$\tilde{P}(\omega)\omega \left[\omega(v^2 - v_d^2) - i\lambda v_d\right] = 0 \tag{1.33}$$

Solving 1.33:

$$\tilde{P}(\omega) = A\ \delta(\omega) + B\ \delta\left(\omega - \frac{i\lambda v_d}{v^2 - v_d^2}\right) \tag{1.34}$$

Enforcing a free-flux condition at $z = 0$ implies $A = 0$. Anti-transforming:

$$P(z) = P_0 e^{-kz} \tag{1.35}$$

$$k = \frac{v_d \lambda}{v^2 - v_d^2} \tag{1.36}$$

where k is the inverse sedimentation length. Eq.(1.35) shares Perrin's format (cf. Eq.1.29) but (1.36) shows the difference respect to a passive colloid.

The sedimentation length k^{-1} tends to zero as $v_d \to v$ for a finite value of F_g, while in the passive case, a null sedimentation length is reached only in the limit $F_g \to \infty$. If $v_d \gg v$ both bacteria groups, $c = 1$ and $c = -1$, experience a net downward motion and a steady state is reached only when all bacteria lie on the bottom.

More generally, considering now $c = cos\theta$, where θ is the angle between the propulsion direction and the vertical Eqs.(1.31) and (1.32) become:

$$P(z)dz = 2\pi \int_{-1}^{1} P(c,z)dzdc \tag{1.37}$$

$$P(c,z)dz = \frac{\lambda}{4\pi} \int_{0}^{\infty} P(z_i(z,c,\tau))dz_i e^{-\lambda\tau} d\tau \tag{1.38}$$

Using the Fourier transform as before:

$$\tilde{P}(\omega) = \tilde{P}(\omega)\frac{\lambda}{\omega v} \int_{0}^{\infty} exp\left(-\frac{\lambda + i\omega v_d}{\omega v}\right) \frac{sin(u)}{u} du \tag{1.39}$$

Solving Eq.(1.39) :

$$\tilde{P}(\omega)\left[\frac{\omega v}{\lambda} - \arctan\left(\frac{\omega v}{\lambda + i\omega v_d}\right)\right] = 0 \tag{1.40}$$

As seen before, the constant solution is excluded by the flux-free boundary condition and $\tilde{P}(\omega) = \delta(\omega - \omega_0)$ where $\omega_0 v/\lambda = \arctan\left(\omega_0 v/\left(\lambda + i\omega_0 v_d\right)\right)$. Anti-transforming, an expression in Perrin's form for $P(z)$ is found, but in this case $\kappa = i\omega_0$ and has to fulfill the condition:

$$\ln\left(\frac{\kappa(v_d + v) + \lambda}{\kappa(v_d - v) + \lambda}\right) = \frac{2\kappa v}{\lambda} \tag{1.41}$$

As shown in the previous case $\kappa^{-1} \to 0$ as $v_d \to v$ while for $v_d \gg v$ the gravitational force effect prevails.

Eq.(1.41) for $v \gg v_d$ can be linearized:

$$\ln\left(\frac{\kappa(v_d + v) + \lambda}{\kappa(v_d - v) + \lambda}\right) = \ln\left(1 - \frac{2\kappa v + \kappa v_d}{\kappa v - 1}\right) = -\frac{2\kappa v + \kappa v_d}{\kappa v - 1} = \frac{2\kappa v}{\lambda} \tag{1.42}$$

Then, from Eq.(1.42) the diffusive behavior is obtained:

$$\kappa = \frac{3\lambda\, v_d}{v^2} = \frac{v_d}{D} \tag{1.43}$$

where $D = v^2/3\lambda$.

The drift speed induced by the gravitational field on bacteria may be estimated as:

$$v_d = \mu \Delta m g \simeq 0.08\,\mu\mathrm{m/s} \tag{1.44}$$

where $g = 9.8\,\mathrm{m}^2/\mathrm{s}$ and, following [22], *E.coli* mobility $\mu = 30\,\mu\mathrm{m}/(\mathrm{s\,pN})$ is computed considering the shape of *E.coli* body as a prolate ellipsoid and the flagellar bundle as helix. The buoyant cell mass is $\Delta m = (\Delta\rho V)$ where $\Delta\rho = \rho_{E.coli} - \rho_{H_2O}$ is the excess density of cell compared to the density of medium and V in the volume of cells. The value $\rho_{E.coli} = 1.160 \pm 0.001\,\mathrm{gr/cm}^3$ used is the measured value in [23]. Eq.(1.44) implies that the sedimentation effect for micro object is very small, then as suggested by the authors of [4] to study bacterial sedimentation, an enhanced external field, such as the field made by centrifuge, can be used. Following this suggestion, the experiment described in Chapter 3 applies a centrifugal field on bacterial suspension to observe sedimentation.

1.5 Effective temperature

In the previous section a model for bacterial sedimentation is described. The expression found for the steady-state probability density, while analogous to Perrin's formula contains a sedimentation length that accounts for the fact that bacteria are active.

The non equilibrium steady state of an active suspension of colloids under gravity field has been recently investigated in [5]. The active particles used are Janus particles of 1 μm diameter, that are self propelled in a solution of hydrogen peroxide, H_2O_2. The surface of a Janus particle is divided into two different sides. One half bead is covered with platinum. The dismutation of H_2O_2 on it provides the propelling power. (Dismutation is a form of redox reaction in which oxidized and reduced forms of a chemical species are produced simultaneously). These particles are, therefore, an artificial model system displaying the characteristic out-of-equilibrium dynamics of an active suspension. In this experiment is used a microfluidic device

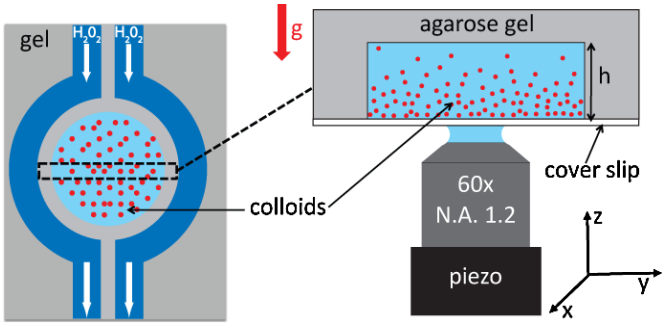

Figure 1.6: Schematic of the microfluidic device used in [5]: on the left there is a top view of the agarose chamber, in gray, while the channels are draw in dark blue. H_2O_2 is pumped into the channels. The agarose chamber contains 1 μm-sized Janus particles, drawn as red spots. The colloidal suspension is observed with a piezo-driven high numerical aperture objective mounted on a inverter microscope (from [5]).

made of agarose gel surrounded by two channels as shown in Fig.1.6. The channels maintain a constant H_2O_2 flux and the gel microsystem permits a constant recharge of H_2O_2 while removing the chemical waste (O_2). Tracking measurements have been done on both passive colloids and Janus particles with and without H_2O_2. Without H_2O_2 Janus particles display a standard diffusive dynamics, while active Janus particles presents a significantly different dynamic from diffusive motion. The motion of this kind of active colloids is described as a persistent random walk, where ballistic motion and angular randomization due to rotational Brownian motion coexist. The measured mean square displacement of a Janus particle, activated by H_2O_2, is described in [5] in terms of an effective diffusion coefficient D_{eff}.

To study sedimentation, Pallacci et al. in [5] have performed a Perrin-like experiment using Janus particles. A single particle tracking and density profile $\rho(z)$, with different oxygen peroxide concentration, are simultaneously measured. Different values of H_2O_2 are considered to measure different particle activity. It was found that the particle activity can be described by D_{eff}. The density profiles exhibit an exponential decay:

$$\rho(z) = \rho_0 \exp(-z/\delta_{\text{eff}}) \tag{1.45}$$

where δ_{eff} is the effective sedimentation length and ρ_0 is a normalization parameter.

In the case of dilute colloids, the flux under gravitational field can be described as:

$$J = -D_{\text{eff}} \nabla \rho + \mu \; m \; g \; \rho \tag{1.46}$$

Eq.(1.46) gives an expression of sedimentation length:

$$\delta_{\text{eff}} = \frac{D_{\text{eff}}}{v_d} \tag{1.47}$$

where $v_d = \mu \Delta m g$ is the sedimentation velocity. The data shown in [5], agree with expression (1.47). Moreover, it was pointed out that this equation can also be interpreted as a measurement of an effective temperature of the system:

$$k_B T_{\text{eff}} = \frac{D_{\text{eff}}}{\mu} = \delta_{\text{eff}} m g \tag{1.48}$$

The effective temperature identified in [5] ranges between ambient temperature and $\sim 10^3 K$.

The experimental results reported in [5] validate the description of active colloids as "hot" colloids, characterized by an effective temperature higher than the temperature of their environment. The description of stationary density distribution in term of an effective diffusion coefficient is applied in Chapter 3 to describe the effects of a centrifugal field on a bacterial suspension.

1.6 Rectification

In recent works [6, 7], it is observed that bacterial motion is rectified by asymmetric obstacles such as the two devices in Fig 1.7. In a microfluidic chamber divided in two partitions by a wall with funnel-shaped openings (Fig. 1.7(a)) a bacterial suspension uniformly distributed at the beginning (see Fig.1.9) after about 1 hour displays an asymmetric density distribution [6]. Moreover, it has been observed in [7] that an asymmetric nanofabricated object immersed in a active bacteria bath rotates spontaneously and unidirectionally (see Figs.1.7(b) and 1.10).

In the wall-of-funnels device, bacteria cross the wall depending on the side in which they are. As shown in Fig 1.8, bacteria coming from the left side of the

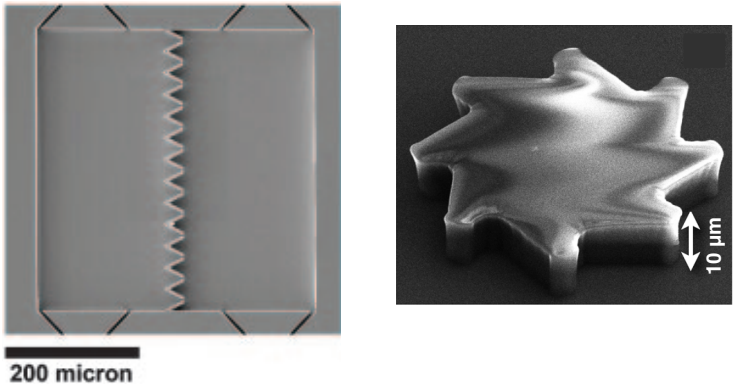

(a) "Wall of funnels" (b) "Ratchet motors"

Figure 1.7: Microdevices: (a) Scanning electron micrograph of device: for create a microfluidic enclosures on silicon wafer microlithography is used. (Figure reproduced from [6]), (b) SEM image of one of the gears used in experiment, the gear external diameter is $48\mu m$ and the thickness is $10\mu m$ [7] (Figure reproduced from [7])

funnel can be driven through the holes between funnels or away from it. On the contrary, bacteria in the right side colliding with the wall are more likely to be strayed away from the gaps. This experiment shows that bacteria approaching the wall align their motion and, losing information on their starting direction, keep the new direction for the entire run also if the wall ends (see Fig.1.8). Near the wall, bacterial moves are biased by the constrained geometry and the run-and-tumble motion gets rectified. The mechanism due to the funnel geometry previously described leads to a concentration of swimming bacteria on the right side of the chamber, as shown in Fig.1.9. In [6], it was observed that the concentration of bacteria on the right side becomes three times larger than that on the left side in about one hour. In [7] differently shaped micro-gears are placed in a bacterial suspension and, depending on the gear geometry, a spontaneous unidirectionally rotation may be observed. To obtain this results, Di Leonardo et al. in [7] have designed an experiment where three important symmetries are broken: time reversal, mirror reflection in a plane through the axis of rotation and half turn about the axis. Bacterial motion, typically out of equilibrium, breaks time reversal. Different shapes of gears are tested in [7] to violate the other two symmetries. As described before, a bacterium, after hits the wall, aligns parallel to the surface of the gear following a direction depending on its

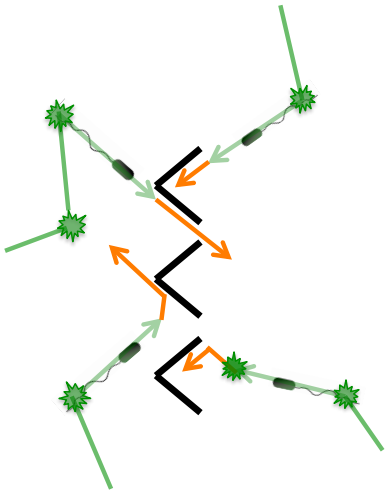

Figure 1.8: Bacteria interactions with funnel walls: coming from the left side bacteria have a chance to go in right side depending on approaching angle, whereas bacteria coming from the right side are more likely to collide with the wall without crossing the gap.

incoming angle. Thus, a bacterium can be locked for a period of time between few seconds and several minutes, during which it pushes the gear, until a tumbling event occurs. In concentrated suspensions, in addition to wall interactions, the repulsion between cells causes a concentration in the corners that results in unidirectional gear rotation. In [7] are explored different shapes and are measured different angular velocities. As expected, symmetric gears just fluctuate with null mean angular speed, and a gear with an opposite orientation gives an opposite rotational direction. The angular velocity of asymmetric gears correlates with bacteria concentration: a larger concentration produces larger average angular speed, but also speed fluctuations become larger.

The above experiments are related to the non-equilibrium feature of active bacteria suspension. It is observed that asymmetric environments are able to lead, without application of external control fields, an out of equilibrium dynamics in a rectified motion. Moreover, the use of asymmetric environments open fascinating perspectives for building microdevices where bacteria could move micro gears or deliver micro

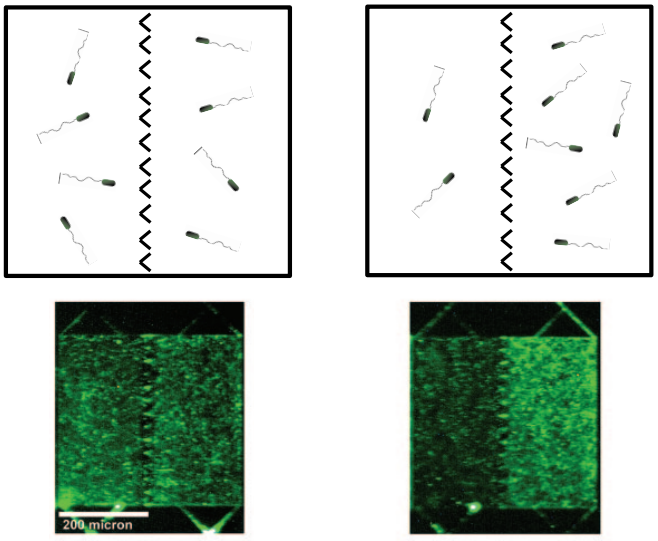

Figure 1.9: Bacteria distribution in the device with funnel walls: (top) schematic representation of the experiment [6]; (bottom) experimental images (from [6]). Bacteria at the beginning are homogeneous distributed in the chamber (bottom left). Bacteria have reached an asymmetric steady state after about one hour (bottom right).

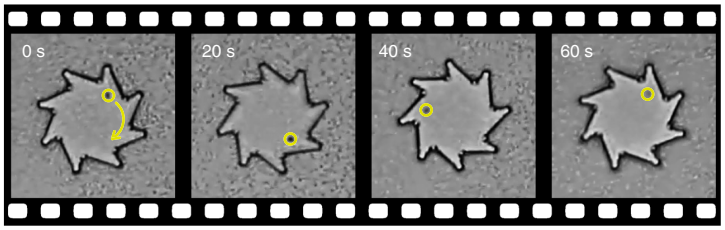

(a) Bacteria-driven micromotor

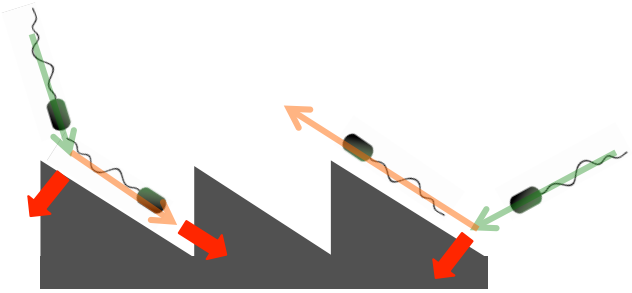

(b) Bacteria interacting with asymmetric boundaries

Figure 1.10: Bacteria ratchet motor: (a) An asymmetric gear in an active bacterial suspension rotates unidirectionally. The angular speed of gear can be measured following the yellow point (from [7]). (b) Schematic of the interaction between bacteria and asymmetric boundaries. Asymmetric teeth rectify bacteria motion. Depending on the incoming angle, bacteria may be trapped in the groove between teeth. Red arrows represent the force applied by bacteria on the wall.

cargos. In Chapter 4, an asymmetric landscape will be used to rectify bacterial motion in order to drive passive colloidal beads.

Chapter 2

Swimming bacteria: *Escherichia coli*

2.1 Introduction

Escherichia coli is one of the most studied bacteria. Discovered in 1885 by the German pediatrician Theodor Escherich, it is easily accessible and suitable to be grown in laboratory. This bacterium usually lives in the lower intestine of warmblooded animals, humans included. The *E.coli* reproduces itself by fission, i.e., subdivision of a cell into two or more parts with the same genetic inheritance. It has a huge number of strains, most of which are not pathogenic. In particular, the strains derived from the *E.coli K-12* is widely used for microbiology studies, being well adapted to laboratory environment and having lost its ability to thrive in the human intestine. One of these strains, namely MG1655, was the first *E.coli* whose DNA sequence was completely decoded in 1997 [24].

In the following sections, we describe the *E.coli* cell, its swimming strategies and we model the forces acting during its motion (Sec.2.2). To perform experiments using bacteria samples, it is important to develop and optimize a correct growth protocol, in order to achieve highly motile *E.coli* samples. Such a protocol is discussed in Sec.2.3. Also the methods used to characterize bacteria samples are important, in order to select cells with well defined and reproducible features. In the last section

we will describe Image Correlation Spectroscopy (ICS), a convenient method for a quick and complete characterization of motility of active samples.

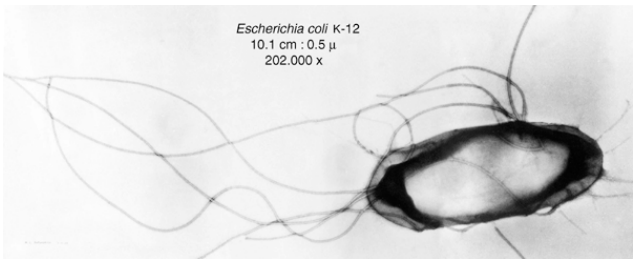

Figure 2.1: Electron micrograph image of *E. coli K-12* by Demphilis and Adler (as reproduced in [25])

2.2 The *E. coli*

Escherichia coli is a rod-shaped bacterium of about 1×2.5 μm that swims using a bundle of helical filaments, called flagella [2](Fig. 2.1). Each flagellum about 20 nm in diameter and several micrometers long is driven by a reversible rotary motor actuated by a proton flux. When all flagella rotate in the same direction, the bacterium is pushed forward. Otherwise, when different flagella rotate in different directions, *E.coli* tumbles randomizing its orientation. Therefore, *E.coli* swims following the same direction for about 1 s (run); then, it moves randomly for about 0.1 s, changing its direction(tumble).

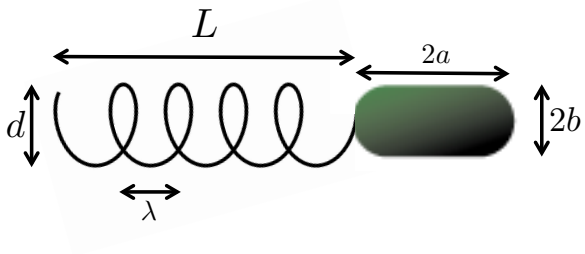

Figure 2.2: A schematic representation of *E.coli*. The body is described as a prolate ellipsoid with $a \simeq 1\mu m$ and $b \simeq 0.5\mu m$. The flagellar bundle is represented as a helix, whose pitch $\lambda \sim 2.5\mu m$ and diameter $d \sim 0.5\mu m$, $L \sim 6 - 10\mu m$.

Flagella are made of the protein flagellin. They exist in several polymorphic forms with different curvatures depending on the arrangement of flagellin filaments (see Fig. 2.3). The filament changes its polymorphic form during the tumble [14]. A normal filament is left-handed, with a pitch of about 2.5 μm and a diameter of about 0.5 μm, its curly filaments are right-handed and have a smaller pitch and diameter. Flagella are in the normal filament form and rotate counterclockwise during a run. When a tumble starts, flagella turn clockwise and the bundle unravels. During this process, the filaments switch from semicoiled to curly form, and come back to normal configuration at the end of the tumbling (Fig. 2.4).

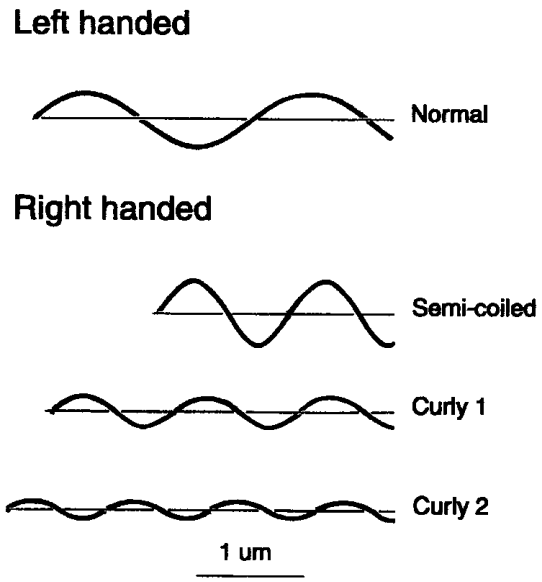

Figure 2.3: Different flagella waveforms. Normal filaments are left handed. On the contrary, semi-coiled, curly1 and curly2 are right handed (Figure reproduced form [14]).

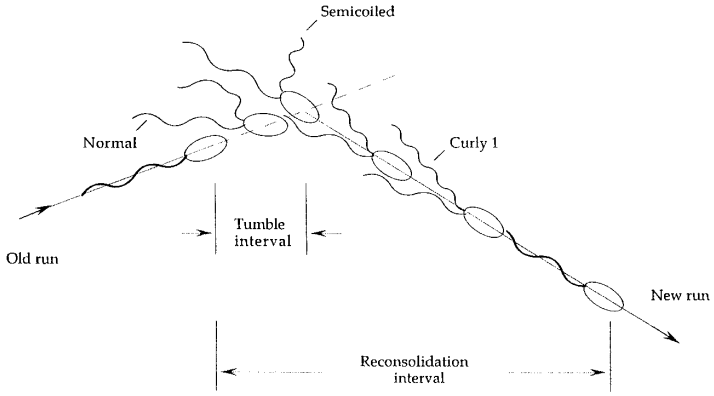

(a) *E.coli* run-and-tumble motion

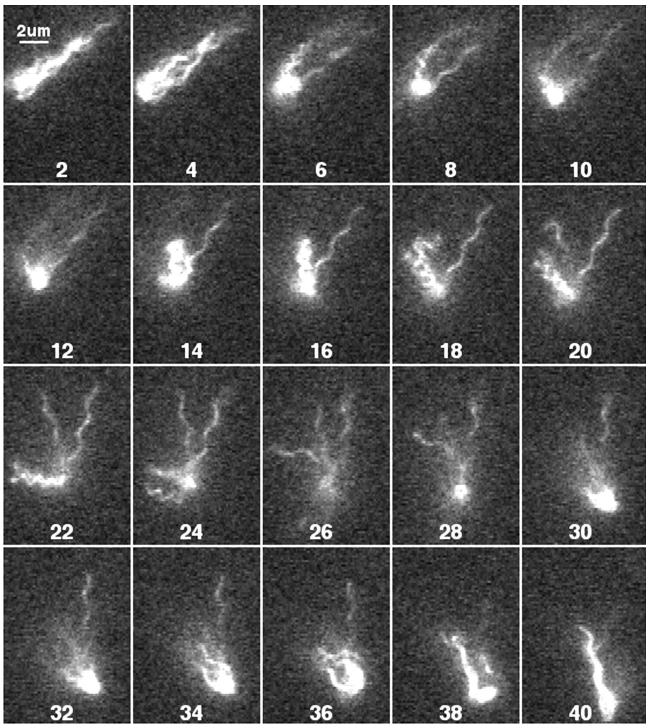

(b) Flagella configurational forms

Figure 2.4: *E.coli* run-and-tumble motion: (a)A *E.coli* runs straight until a flagellum starts to rotate differently from others, changing its form normal to semicoiled and from semicoiled to curly1. At the beginning of a new run flagella come back to their normal form (Figure reproduced from [2]); (b) Frames of fluorescent *E.coli* at progressive time in which filaments take different polymorphic configurations. In this sequence the cell tumbles, changing its original orientation (Figure reproduced from [14]).

2.3 The *E.coli* growth protocol

The procedure for growing *E.coli* bacteria is easy enough to make this bacteria one of the most studied in microbiology. The bacteria colonies growth procedure divides essentially into two steps:

1. Overnight static growth in a liquid growth medium at 33°C;
2. "Synchronization" growth phase in fresh medium, mildly shaken at 200 rpm, for about 4 hours at 33°C.

In the first step a single bacterial colony is taken from a Petri dish and is inoculated in a liquid growth medium. Two typical Petri dishes are shown in Fig.2.5.

After the overnight growth, the culture medium is saturated: the nutrients are almost exhausted and the cells are in different growth stages. Then, the saturated culture is diluted 1 : 100 in a fresh medium. In the second step, mildly shaking produces a uniform distribution of nutrients which leads to the synchronization of cells growth [27]. After the growth process is over, bacterial cells are harvested from the medium by centrifugation at 2000 rpm for 10 min at room temperature. The resulting pellet is gently resuspended by mixing it in a pre-warmed motility buffer [10]. This process is repeated three times, in order to replace the growth medium with a motility buffer and halt bacterial growth. Many physical and chemical factors should be considered to optimize *E.coli* growth. Adler and Templeton studied extensively the effect of environmental conditions on the motility of *E.coli* [10]. The most used growth and motility medium are chosen according to their results. The best growth media is a mixture of 20 aminoacids commonly found in proteins, such as those included in tryptone. *E.coli* can grow at a temperature between 24°C and 37°C, temperatures above 37°C should be avoided to have proper flagellar synthesis. The proper pH range is between 6.0 and 8.0. To preserve bacteria motility, it is important to replace the growth medium with an appropriate buffer. Adler and Templeton found that glucose is a proper energy source. However, it needs a chelating chemical agent such as EDTA, to prevent the reduction in motility due to traces of heavy metal ion in water solution. A motility buffer consist of phosphate buffer (pH 7, 10^{-2} M), glucose 10^{-2} M and EDTA 10^{-4} M preserve a good motility in an *E.coli* sample. Phosphate buffer is used to maintain an optimum pH value,

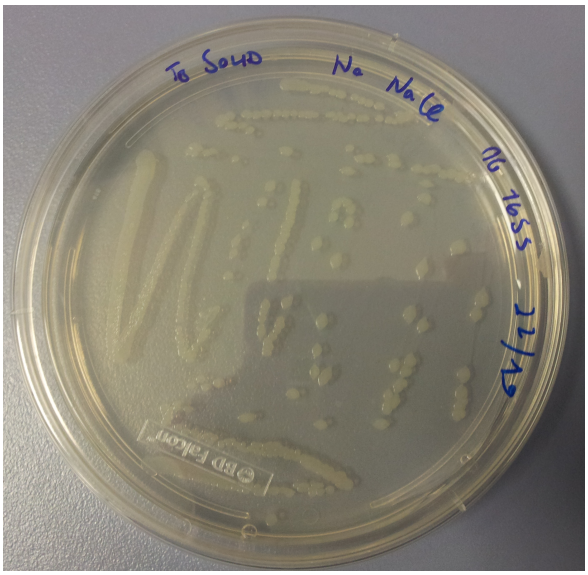

(a) Petri dish of *E.coli* MG 1655

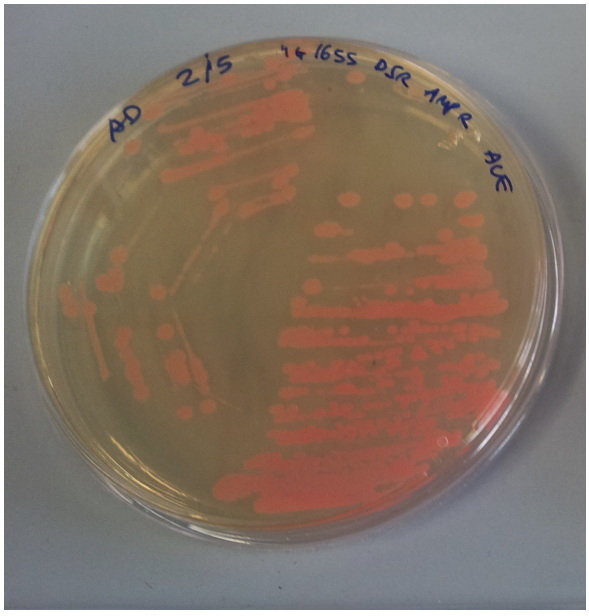

(b) Petri dish of *E.coli* MG 1655 DsRed

Figure 2.5: *E.coli* colonies grown on Petri dish. (a) *E.coli* MG1655 colonies, (b) *E.coli* colonies labelled with fluorescent red protein (DsRed). Single colonies are the white and pink spots on Petri, respectively. The Petri dish contains a mixture of 1% trypton and 1.5% of Agar.

between 6 and 7.5. It can be replaced with other similar buffers with the same pH value. A pH value of $3-4$ must be avoided, otherwise flagella break. *E.coli* are able to grow both in aerobic and anaerobic conditions. Tryptone broth and glucose motility buffer also allow anaerobic motion. However, their speed is smaller than in aerobic conditions.

2.3.1 The growth curve

To follow the *E.coli* growth in time it is useful to harvest motile and active cells from the culture. The generation time of a bacterial population is obtained measuring the Optical Density (OD) i.e., the logarithm of the ratio between the intensity of the incident radiation and of the transmitted radiation through a material, which is proportional to the density of scatterers. The growth curve obtained measuring the increase of *E.coli* density in time, may be sub-divided into four different phases (Fig. 2.6). During the Lag phase, immediately after the inoculation of bacterial cells into

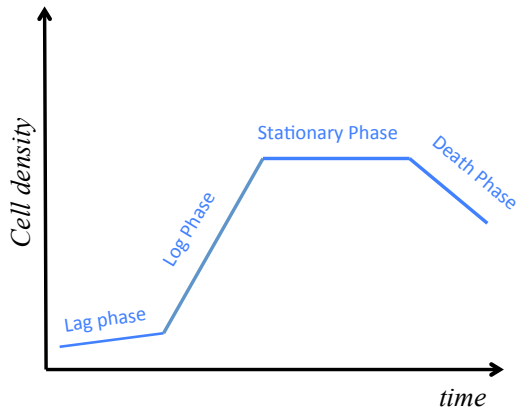

Figure 2.6: A schematic growth curve highlighting the four growth phases.

a fresh medium, the number of cells does not change. The duration of this phase corresponds to the time necessary for bacteria to adapt to growth condition.
In Logarithmic or Exponential phase, bacteria grow normally going through a binary division: each cell divides into two daughter cells with the same genetic stock. In this phase, the number of *E.coli* cells increases as $n_0 2^{t/\tau}$ where τ is the generation time and n_0 is the starting number of bacteria; if the nutrient were unlimited this kind of growth would last forever.

In a finite volume of growth medium, the nutrient decreases as the number of bacteria increases, and the culture reaches the Stationary phase in which growth and death rates are equal. In the Death phase, nutrients are exhausted and bacteria die. An OD measurement in enable to detect this phase, since absorbance does not discriminate between live and dead cells.

In a quantitative description of the entire growth procedure, it is important to consider the starting number of bacteria in the culture, n_0, and the number of bacteria in the saturation phase, n_s.

When growth begins, $\frac{dN(t)}{dt} = rN(t)$ where r is the growth rate.

For $t \to \infty : N(t) \to n_s$. According to these observations:

$$\frac{dN(t)}{dt} = rN(t)\left(1 - \frac{N(t)}{n_s}\right) \tag{2.1}$$

Integrating Eq.2.1 yields:

$$N(t) = \frac{n_0 n_s}{n_0 + (n_s - n_0)\, e^{t/\tau}} \tag{2.2}$$

Equation (2.2) is the logistic equation describing the population growth, originally derived by Verhulst. The *E.coli* growth rate is $\frac{\ln 2}{\tau}$, therefore Eq.(2.2) may be rewritten in the form:

$$n(t) = \frac{n_0 n_s}{n_0 + (n_s - n_0)\, 2^{t/\tau}} \tag{2.3}$$

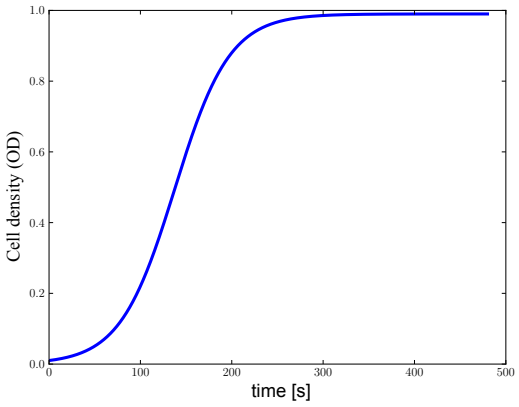

Figure 2.7: The growth curve of *E.coli* as obtained from the logistic equation (2.3)

2.4 Motility characterization

In biology, motility is defined as the ability to move spontaneously and actively, consuming energy during the process. At the cell level, there are different types of motility such as flagellar motility [28], amoeboid motion [29] and swarming [30]. Motility characteristics can be modulated in response to environmental conditions [10]. In particular, flagellar motility plays an important role in the motion of prokaryotic and eukaryotic organisms [31]. Developing a method to characterize bacteria samples is necessary to quantify sample features such as cells speed and the fraction of motile cells. In his pioneering work, Adler, see Sec.2.3, used a method based on capillary tubes to select the best growth and motility media [32]. This method measures the distribution of the displacement of bacteria colonies in time in capillary tubes filled with a motility medium. It estimates empirically the motility of bacterial colonies in certain motility medium, but does not give a measure of bacteria speed. Moreover, this procedure takes several hours.

2.4.1 Tracking

A more detailed method is based on tracking individual trajectories. In principle, this method can be used for a ensemble of N particles, each with a trajectory $\mathbf{s}_i(t)$ where $0 \leq i \leq N$, computes the particle velocity as:

$$\mathbf{v}_i(t) \simeq \frac{\mathbf{s}_i(t+\delta t) - \mathbf{s}_i(t)}{\delta t} \tag{2.4}$$

where the time step δt between two consecutive particle positions is chosen according to the temporal scale of motion. Berg and collaborators have made a microscope to track a single bacteria in 3D [2, 33]. This microscope allows the 3D tracking using a servo-control system keeping a single cell in focus [34]. Using this method, Berg measured the *E.coli* trajectories along x, y and z axis, as shown in Fig.2.8. This tracking measurements have permitted to quantify the run-and-tumble motion of *E.coli* [33]. A 2D tracking method requires a simpler equipment than the 3D tracking and can be used to characterize the motility of samples confined in a thin layer, such as a thin bacteria suspension. Instead, collecting a sequence of images with a ccd camera, it is possible to follow the bacteria trajectories. The tracking process depends on particle visibility in the microscope and requires a low density

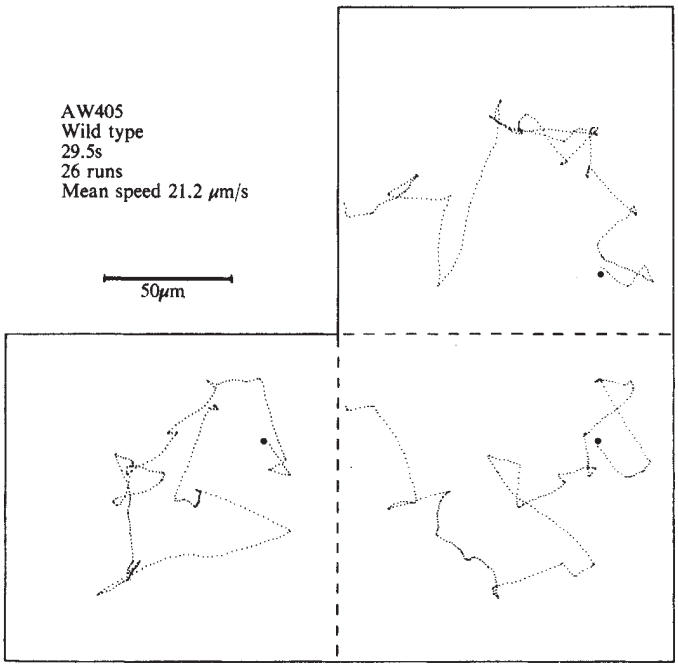

Figure 2.8: Planar projections of the *E.coli* wild type of 3D trajectories acquired with a Berg microscope (figure reproduced from [33]).

sample to follow precisely individual particles. Therefore, tracking is restricted to low density samples. Moreover, it may needs that image contrast to be improved, particularly for bacterial samples.

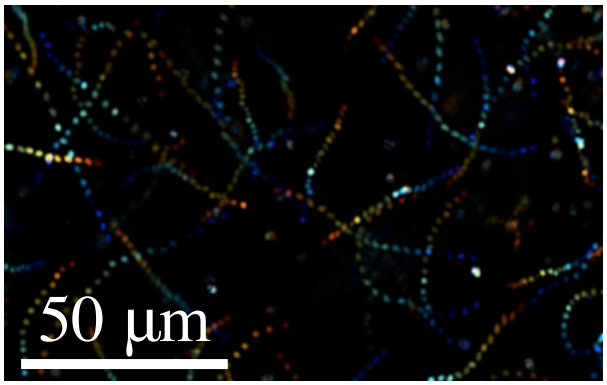

Figure 2.9: An example of tracked swimming *E.coli* cells. Traces are obtained by superposing of frames that have been colored progressively from red to blue as time increases.

2.4.2 Differential Dynamic Microscopy (DDM) and Image Correlation Spectroscopy (ICS)

Recently two methods, namely Differential Dynamic microscopy (DDM)[35] and Image Correlation Spectroscopy (ICS)[36], have been proposed to characterize the motility of microorganisms. DDM and ICS methods provide statistics larger than the tracking method, averaging over thousand of particles in a few minutes and performing a Fourier analysis of collected digital images [11, 37]. Both methods compute the same quantity accessible to Dynamic Light Scattering (DLS) [38] i.e. the Intermediate Scattering Function, ISF.
The intermediated scattering function is defined as follows [38]:

$$F(q,t) = N^{-1} \sum_{j=1}^{N} \langle \exp[i\,\mathbf{q} \cdot (\mathbf{r}_j(t) - \mathbf{r}_j(0))] \rangle \tag{2.5}$$

where $\mathbf{r}_j(t)$ is the position of the $j-$th particle at time t; the sum is extended to all the N identical and non-interacting particles of the sample and $\mathbf{q}$ is the scattering vector. The ISF is the Fourier transform of the self-correlation function of the instantaneous microscopic density in the sample. In fact, (2.5) may be rewritten as:

$$F(\mathbf{q},t) = \langle \rho(\mathbf{q},0)\rho(\mathbf{q},t) \rangle \tag{2.6}$$

where $\rho(\mathbf{q},t) = \sum_{j=1}^{N} \exp(\mathbf{q} \cdot \mathbf{r}_j(t))$ is the Fourier transform of the sample instantaneous microscopic density. The advantage of DDM and ICS is that the interesting q-range to study bacteria motion is easily accessible and a complete set of q can be derived with only a measurement.

2.5 Image Correlation Spectroscopy

An image is described by the intensity $I(\vec{r},t)$ in a point $\vec{r}$ at time t. In a sample of colloidal particles, $I(\vec{r},t)$ fluctuates with time. Therefore, dynamical information about particle motion can be derived by studying the correlation function of the intensity in time.

The image correlation function $g(\mathbf{q}, t, t')$ is:

$$g(\mathbf{q}, t, t') = \langle I^*(\mathbf{q}, t')\, I(\mathbf{q}, t' + t)\rangle, \tag{2.7}$$

where $I(\mathbf{q}, t)$ is the spatial Fourier transform of the image $I(\mathbf{r}, t)$ at the wave-vector $\mathbf{q}$ and star denotes complex conjugate.
In a quasi-stationary system, within the measurement time $g(\mathbf{q}, t, t') = g(\mathbf{q}, t)$ and therefore it is possible to average over time-origins t'. Moreover, assuming an isotropic sample, $g(\mathbf{q}, t)$ can be written as function of $q = |\mathbf{q}|$, i.e. $g(\mathbf{q}, t) = g(q, t)$, so that function can be averaged over all $\mathbf{q}$-vectors having the same magnitude. The correlation function under this assumptions becomes:

$$g(q, t) = \langle I^*(q, 0)\, I(q, t)\rangle. \tag{2.8}$$

In Fourier space a general intensity profile of scattered light from a colloidal sample can be written as a sum over N objects in the sample, each of them described by its form factor $b(\mathbf{q}, t)$ times the position where the $i - th$ object is:

$$I(\mathbf{q}, t) = \sum_{i}^{N} \hat{b}_i(\mathbf{q}) e^{i\mathbf{q}\mathbf{r_i}(t)}. \tag{2.9}$$

The correlation function is described by:

$$\langle I^*(q, 0)\, I(q, t)\rangle = \langle \sum_{i,j}^{N} \hat{b}_i^*(q) \hat{b}_j(q) e^{iq(r_j(t) - r_i(0))}\rangle. \tag{2.10}$$

Considering that each particle has the same form factor and for $i = j$:

$$\langle I^*(q, 0)\, I(q, t)\rangle = \langle \sum_{i}^{N} |\hat{b}_i(q)|^2 e^{iq(r_i(t) - r_i(0))}\rangle. \tag{2.11}$$

For non-interacting particles, the function $g(q, t)$ is related to the self-intermediate scattering function $F(q, t)$ (shown in Eq. (2.5)). So, the image correlation function can be rewritten as

$$g(q, t) = A(q)\, F(q, t) + B(q), \tag{2.12}$$

$A(q)$ and $B(q)$ are time-independent factors depending, respectively, on the average (static) structure of the image and on the background noise. $B(q)$ contains also contributions from static objects on the image.

2.5.1 Intermediate Scattering Function (ISF) of motile microorganisms

The Intermediated Scattering Function, $F(q,t)$, can be used to describe a swimming microorganism like *E.coli* [38, 39], by assuming that on the relevant length-scales $\sim q^{-1}$ swimming bacteria move with speed v along straight trajectories in 3D.
Considering the velocity distribution of bacteria $P(\mathbf{v})$:

$$F(\mathbf{q},t) = \int d^3\mathbf{v} P(\mathbf{v}) \exp(i\mathbf{q}\mathbf{v}t) \tag{2.13}$$

where $\mathbf{v}t = \mathbf{r}(t) - \mathbf{r}(0)$.
Integrating (2.13) in polar coordinates and choosing a reference system in which $\mathbf{q}$ is parallel to the z axis:

$$F(q,t) = \int_0^{2\pi} d\phi \int_0^{\pi} d\theta \sin\theta \int_0^{\infty} dv v^2 P(v) \exp(i\, q\, v\, t\, \cos\theta) \tag{2.14}$$

Bacteria trajectories are equiprobable, therefore $P(\mathbf{v}) = P(|v|)$. Then, the angular integration of Eq.(2.14) yields

$$F(q,t) = 4\pi \int_0^{\infty} dv v^2 P(v) \frac{\sin qvt}{qvt}. \tag{2.15}$$

In addition, bacteria are subject to Brownian motion characterized by a diffusion coefficient D. This thermal motion alone would give $F(q,t) = \exp(-q^2 Dt)$. This expression can be derived introducing the Van-Hove function [38]:

$$G(\mathbf{R},t) = \langle \delta(\mathbf{R} - [\mathbf{r_j}(t) - \mathbf{r_j}(0)] \rangle \tag{2.16}$$

$G(\mathbf{R},t)$ is related to the probability distribution for a particle to undergo a displacement $\mathbf{R}$. The ISF and Van-Hove functions are related by a Fourier transform:

$$F(\mathbf{q},t) = \int d^3R\, G(\mathbf{R},t) e^{iq\mathbf{R}}. \tag{2.17}$$

The $G(\mathbf{R},t)$ can be considered as the solution of the diffusion equation

$$\frac{\partial}{\partial t}G(\mathbf{R},t) = D\nabla^2 G(\mathbf{R},t). \tag{2.18}$$

Transforming it by Fourier:

$$\frac{\partial}{\partial t}F(\mathbf{q},t) = -q^2 D\nabla^2 F(\mathbf{q},t). \tag{2.19}$$

For Brownian particle $G(\mathbf{R},0) = \delta(\mathbf{R})$ and $F(\mathbf{q},0) = 1$, then the solution of (2.19) becomes $F(q,t) = \exp(-q^2 Dt)$. Combining these two dynamical processes and considering that in a sample only a fraction of α motile cells is present:

$$F(q,t) = e^{-q^2 Dt}\left[4\pi\alpha\int_0^\infty dv\, P(v)\,\mathrm{sinc}(qvt) + (1-\alpha)\right] \tag{2.20}$$

where $P(v)\,dv$ is the probability of finding a bacterium with speed between v and $v+dv$.

In previous works [37, 39], in order to fit experimental data, the $P(v)$ was modeled with a Schulz distribution:

$$P(v) = \frac{v^Z}{Z!}\left(\frac{Z+1}{\langle v\rangle}\right)^{Z+1}\exp\left[-\frac{v}{\langle v\rangle}(Z+1)\right] \tag{2.21}$$

where Z depends on the variance $\sigma = \langle v\rangle(Z+1)^{-1/2}$. Fig.2.10 shows the Schulz distribution with $\langle v\rangle = 15\mu$m/s and $\sigma = 7\mu$m/s.

Fig.2.11 shows the $F(q,t)$ of a typical bacterial population modeled by Eq.(2.20). The top chart are shows $F(q,t)$ (solid line) for $q = 0.77\mu\mathrm{m}^{-1}$ and its swimming and diffusive components (dashed lines). The bottom chart shows a $F(q,t)$ for a set of q-values. Fig.2.12 shows an experimental $F(q,t)$ computed from image correlation function $g(q,t)$ via Eq.(2.12). The reconstructed $F(q,t)$ is well described by Eq.(2.20), where $P(v)$ is modeled by Eq.(2.21).

2.6 Motility characterization of *E.coli* suspensions

Motility characterization by ICS requires only a microscope, a ccd camera with a high fps (frame per second) and a computer to analyze the data (Fig.2.13). A

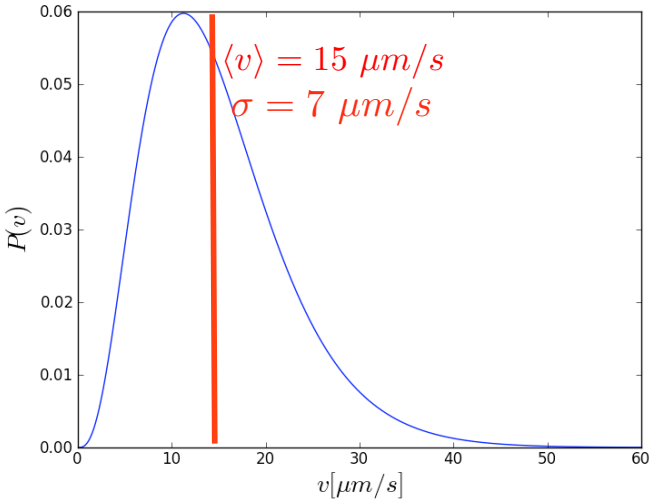

Figure 2.10: Schulz distribution with $\langle v \rangle = 15\mu$m/s and $\sigma = 7\mu$m/s. The vertical red bar denotes the value of $\langle v \rangle$.

bacterial sample satisfies the assumptions of quasi-stationarity and isotropy made on the image correlation function $g(q,t)$ (see Sec.2.5). In fact, quasi-stationarity is due to a measurement time much larger then characteristic times of probed system and the isotropy is due by bacterial motion which trajectories are randomize in all directions. Data analysis consists in the computation of $g(q,t)$ and in the estimation, via a fitting procedure, of the six parameters $A(q), B(q), D, \alpha, \sigma, \langle v \rangle$.

2.6.1 The q-range

To extract motility parameters from the Intermediate Scattering Function, it is necessary to measure this function in an proper q-range.

The experimental q_{min}^{exp} depending on the camera spatial resolution and on image size L in pixel. Hamamatsu CMOS camera have a pixel size of $3.63 \times 3.63\,\mu$m, with a $10\times$ magnification, the inverse pixel size is $k = .363\,\mu\text{m}^{-1}$. Therefore:

$$q_{min}^{exp} = \frac{2\pi k}{L} \simeq 0.01\mu\text{m}^{-1} \tag{2.22}$$

where $L = 256$ pixels was chosen according to the smallest dimension of the analyzed images. The value of $q_{max}^{exp} \simeq 2.2\mu\text{m}^{-1}$ is evaluated considering the smallest size, $L =$

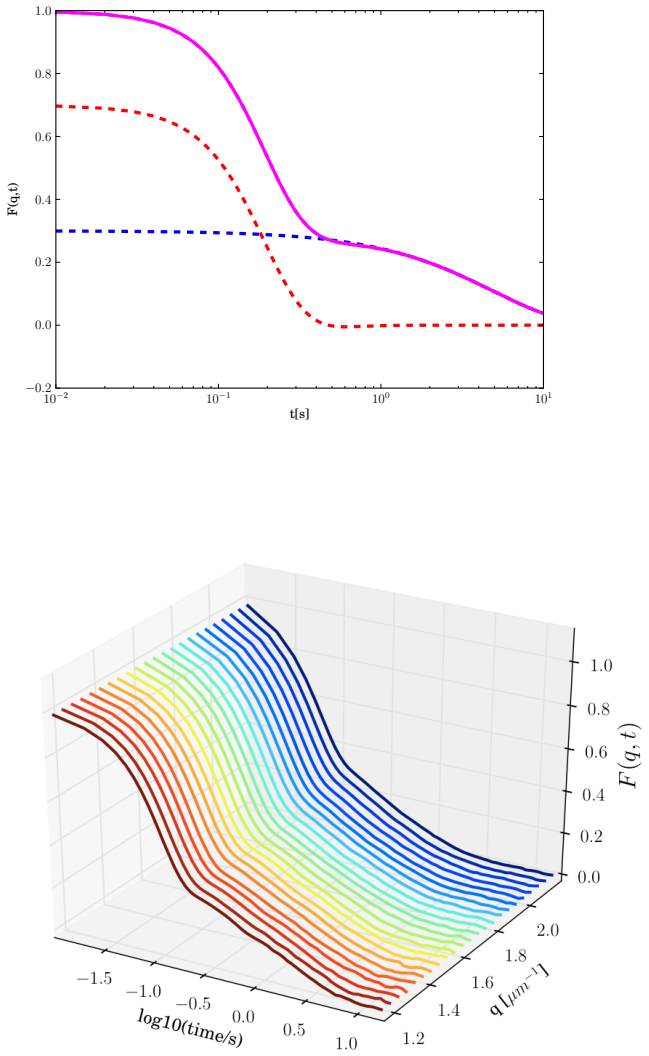

Figure 2.11: Intermediate Scattering Function $F(q,t)$ of a bacterial suspension: (top) the solid line is the $F(q,t)(q = 0.77\mu\text{m}^{-1})$, the dotted lines represent the swimming (red) and the diffusive component (blue) of $F(q,t)$. (bottom)$F(q,t)$ for a set of q-values ($1.2\mu\text{m}^{-1} \ll q \ll 2.2\mu\text{m}^{-1}$). The ISF is computed for a population of *E.coli* characterised by: $\langle v \rangle = 15\mu\text{ms}^{-1}$, $\sigma = 7\mu\text{ms}^{-1}$, $D = 0.35\mu\text{m}^2\text{s}^{-1}$ and $\alpha = 0.7$, $P(v)$ is modeled by a Schulz distribution.

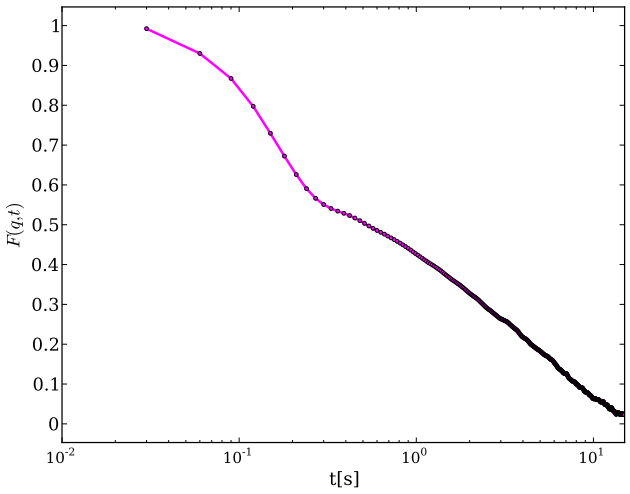

Figure 2.12: Intermediate scattering function $F(q,t)$ ($q = 0.77\mu\text{m}^{-1}$) obtained by experimental data of an *E.coli* sample. The solid line is the fitted function with Eq.(2.20).

1 pixel. Then the q-range experimentally accessible is $0.01\mu\text{m}^{-1} \leq q \leq 2.2\,\mu\text{m}^{-1}$. To extract the motility parameters of *E.coli* suspensions from measurements, it is important to know the q-range relevant for bacterial dynamics. An upper limit is due by *E.coli* size :

$$q_{max}^{E.coli} \simeq \frac{2\pi}{a} \simeq 6\mu\text{m}^{-1} \tag{2.23}$$

with $a \sim 1\mu$m is typical cell size, whereas, to include larger scale as bacteria runs:

$$q_{min}^{E.coli} \simeq \frac{2\pi}{l_{run}} \simeq 0.5\mu\text{m}^{-1} \tag{2.24}$$

with $l_{run} \sim 10\mu$m in our *E.coli* sample. Thus, in the range $0.5 \leq q^{E.coli} \leq 6\mu\text{m}^{-1}$ an *E.coli* population can be modeled.
Consider both q^{exp} and $q^{E.coli}$ range, an appropriate q-range can be:

$$0.5\mu\text{m}^{-1} \leq q \leq 2.2\mu\text{m}^{-1} \tag{2.25}$$

Fig.2.14 shows the fitted parameter $A(q)$, $B(q)$, D, α, σ, $\langle v \rangle$ from Eqs. (2.20) and (2.21) in the proper q-range to study bacteria samples. Those motility parameters

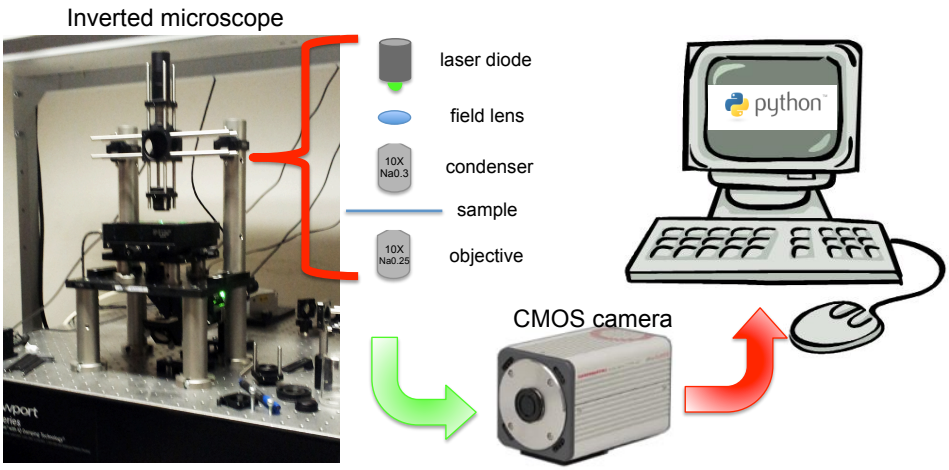

Figure 2.13: Schematic of the equipment used to perform an ICS analysis. In our laboratories we use an inverted microscope, we collect the images by CMOS camera (Hamamatsu Orca Flash 2.8 [40]) and we perform the analysis with a computer software written in Python [41].

are all independent of q, for a value $q > 1\mu\text{m}^{-1}$. The typical motility parameters, averaged over q, of our bacteria samples, are: $\langle v \rangle_q = 10.2 \pm 0.4 \mu\text{ms}^{-1}$, $\alpha = 0.9 \pm 0.1$, $D = 0.31 \pm 0.01 \mu\text{m}^2\text{s}^{-1}$, $\sigma = 9.8 \pm 0.5 \mu\text{ms}^{-1}$.

2.6.2 Results

We used the ICS method to better understand and to improve the growth protocol of our *E.coli* colonies. A first investigation was intended to find the optimal condition to halt growth and to collect the cells when bacteria are highly motile. In this case, we measure the OD of culture cells in the growth medium every 20 minutes, using a spectrophotometer. To perform the ICS analysis, the images (512 × 512 pixel) are collected at 50 fps (frame per second) by a CMOS camera (Hamamatsu Orca Flash 2.8 [40]), for 10 seconds (∼ 500 frames).

E.coli cells (MG1655) are grown overnight at 33 °C in tryptone broth (Fluka) containing 1% tryptone and 0.5 % NaCl. The saturated culture is then diluted 1:100 into a fresh medium and shaken at 200 r.p.m. We measure the OD and collect the

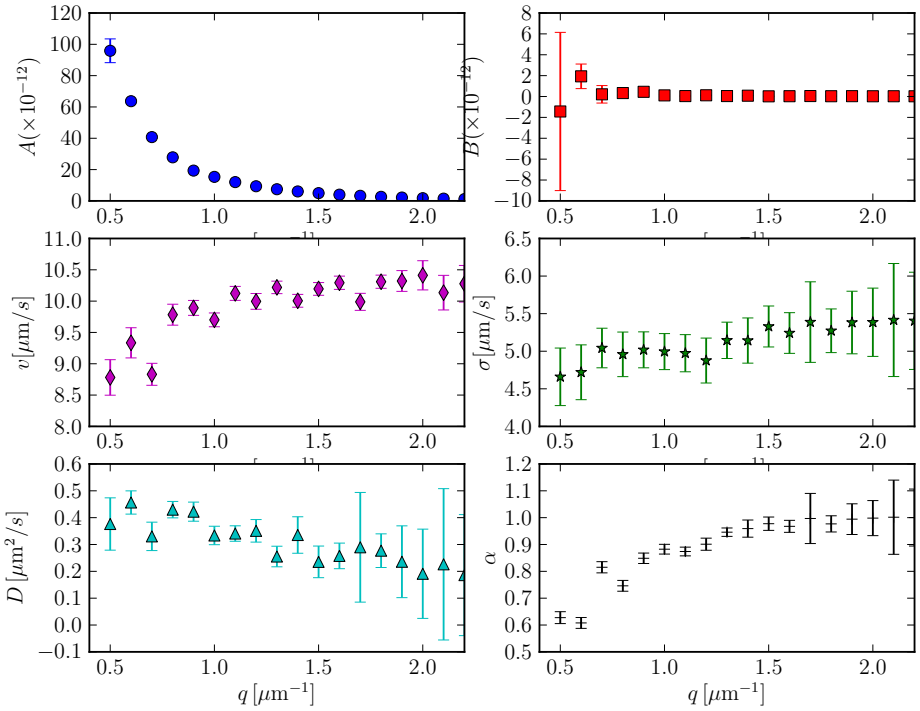

Figure 2.14: Fitting parameter values in the q-range between 0.5 and 2.2μm^{-1}.

images of the *E.coli* culture every 20 minutes during growth. As shown in Fig.2.15, the cells reach the maximum swimming speed after 4 hours. In our *E.coli* growth curve this time interval corresponds approximately to the mid point of the exponential phase.

It is also interesting to measure the fraction of motile bacteria, α, during the growth process. In Fig.2.16, α values are compared to the mean speed averaged over q. The maximum fraction of motile cells is reached for $\langle v \rangle_q^{max} = 15\mu$ms^{-1}, whereas the value of α corresponding to the maximum swimming speed is ~ 0.7. This value is typical of *E.coli* suspensions used in experiments [37, 39]. To obtain an *E.coli* sample composed of a larger fraction of motile cells, the cells should be harvested from the culture after 3.5 h, when bacteria swim at $\sim 15\mu$ms^{-1} and $\alpha \sim 1$.
We have chosen to collect bacteria from the culture medium after 4 hours, since this duration yields the best compromise between motility and fraction of motile cells.

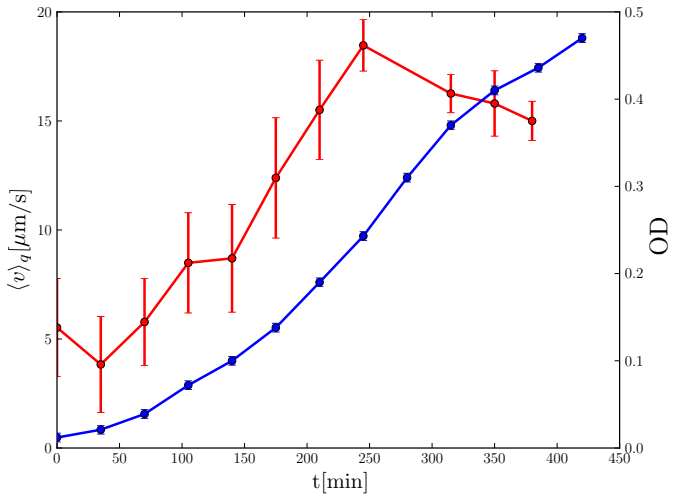

Figure 2.15: The red solid line is the mean speed averaged over q, the blue is the OD of the *E.coli* sample as a function of growth time. In the OD measurements, the error is within the size of the circle marker in the figure.

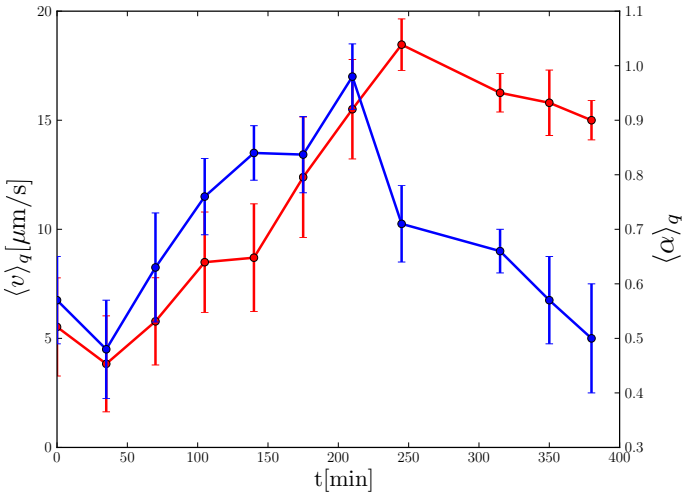

Figure 2.16: The mean speed (red) and α (blue) averaged over q of *E.coli* sample as a function of growth time.

We also test the average swimming speed as a function of the time elapsed, after the sample was sealed in a capillary. The *E.coli* cells are grown as described above, and

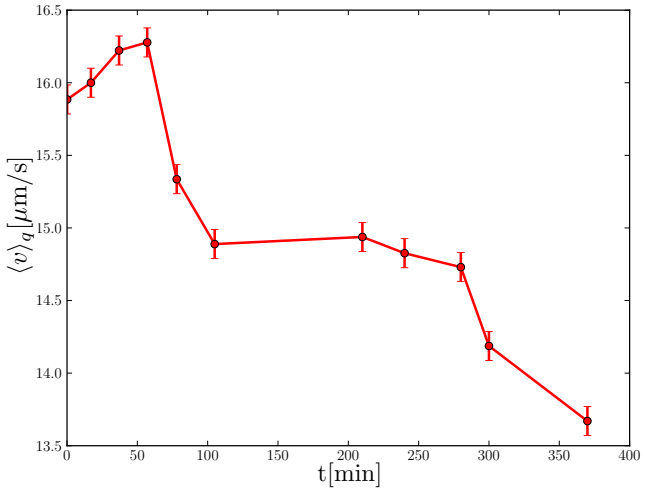

Figure 2.17: The q-average speed of a sealed *E.coli* sample as a function of time.

after 4 hours the cells are harvested from culture media by centrifugation at 2000 rpm for 10 minutes at room temperature. The pellet is resuspended by gently mixing in a pre-warmed motility buffer composed of 10 mM potassium phosphate, 0.1 mM Na-EDTA (pH 7.0), 76 mM NaCl and 0.002% Tween-20. To seal the samples, we use an adhesive wax (VALAP). VALAP is a biological inert compound, composed by VAselline, LAnolin and Paraffine mixed together in equal parts by weight [42]. The average mean speed decreases after the first 50 minutes after the sealing, until it reaches a plateaux between 100 and 250 minutes and finally decreases down to a value around 13.5μm/s after about 6 hours, as shown in Fig.2.17.

Chapter 3

E. coli in a centrifugal field: motility fractionation

3.1 Introduction

In this chapter, investigating the effects of an external centrifugal field on bacteria suspensions, we will demonstrate that centrifugation can be used efficiently to separate swimming cells having different motility [8].

Centrifugation is part of ordinary laboratory technique, commonly used to separate mixtures into fractions characterized by specific size, weight or density. This process using centrifugal force leads to the sedimentation of different components in a mixture. Usually, centrifugation is useful to separate quickly two different components being carried out at high rpm (rotations per minute) and leading to a dense packed pellet. Choosing an appropriate centrifugal acceleration it is possible to use the centrifugal force to observe the sedimentation effects.

When a steady state is reached, each component of the mixture has a Boltzmann density distribution

$$\rho(z) \propto \exp\left[-v_d z/D\right] \tag{3.1}$$

the drift speed $v_d = \mu \Delta m a$ is induced by a uniform centrifugal acceleration a on a particle having a buoyant mass Δm, mobility μ and a diffusion coefficient D.

Bacteria are self-propelled cells far from equilibrium, as pointed out in Secs. 1.3-

1.5. It has been observed [5], that, for active colloidal particles, sedimentation can be described by an effective diffusion coefficient. Consequently, also in this case, we can consider bacteria as "hot colloids" and their diffusion as an effective diffusion depending on motility.

However, centrifugation may be used also to sort bacteria according to their motility. As pointed out in Sec. 2.4, characterizing bacteria motility is an important task for preparing a sample with controlled features. Image correlation techniques such as Image Correlation Spectroscopy (ICS) and Differential Dynamic Microscopy(DDM) are powerful tools to characterize the motility of microorganisms, as described in Sec. 2.5. Beyond the characterization, also the development of methods aimed at sorting bacteria colonies with selected motility is interesting for physics and microbiology purposes. Field-flow fractionation has been used to isolate motile nonchemotactic *E.coli* from a mixture of strains having different phenotypes [43]. Recently, advances in micro-fabrication techniques have led to the development of microstructures that can concentrate motile cells [6, 44] and sort them according to their length [45]. Some examples of these micro-devices are shown in Fig. 3.1. These devices, while are useful to separate cells with different characteristic, are not able to quantify bacterial motility. Instead, combining centrifugation tools and Image Correlation Spectroscopy, we are able to measure the space-resolved motility distribution under the effect of centrifugal field in the range $\sim 4g - 12g$.

3.2 Experiment

3.2.1 Experimental setup

The experimental setup is designed to combine a dark-field microscope with a centrifugation apparatus as shown in Fig. 3.2. In dark-field microscopy, the incoming light is partially blocked by a beam stopper before entering in the condenser objective. Only the rays on the edge are focused on the sample. Therefore, only scattered light is collected by the imaging objective. Dark-field microscopy permits the acquisition of well-contrasted sample images composed of bright objects against a dark background [46]. In Fig. 3.3 the image of an *E.coli* sample acquired with dark microscopy is compared with the image of a similar sample recorded in bright-field

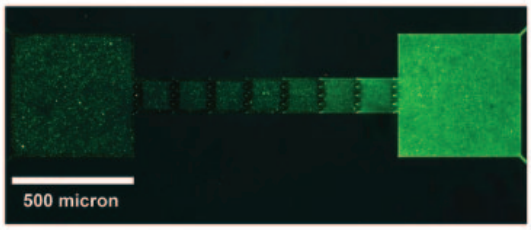

(a) Funnels pump

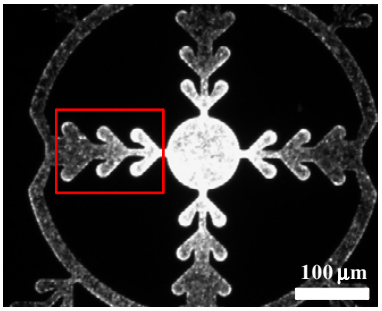

(b) Bacteria concentator

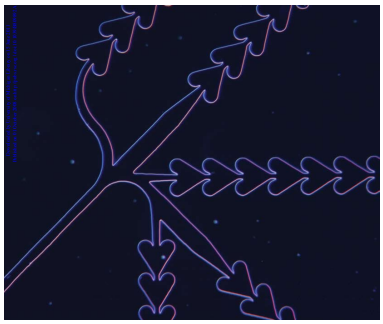

(c) Microfluidic sorting cells device

Figure 3.1: Microfluidic devices for concentrating and sorting cells: (a)An array of funnels acting as a pump to concentrate motile cells in a chamber. The device is fabricated by microlithography (figure reproduced from [6]). (b)Motile cell concentrator fabricated with standard soft lithography. The concentrator consists of a central chamber and four arrays of arrowhead-shaped structures. Cells in the circular channel are forced to move into the arrowhead-shaped structures by the protruding wall (figure reproduced from [44]). (c)Microfluidic device developed to sort cells by length: the four arrowhead-shaped channel are able to separate and select the younger (hence, the smaller) cells taking avail of the hydrodynamic interactions between bacteria and the microchannel geometry. An *E.coli* strain labelled with green fluorescent protein (GFP) was used in all these experiments.

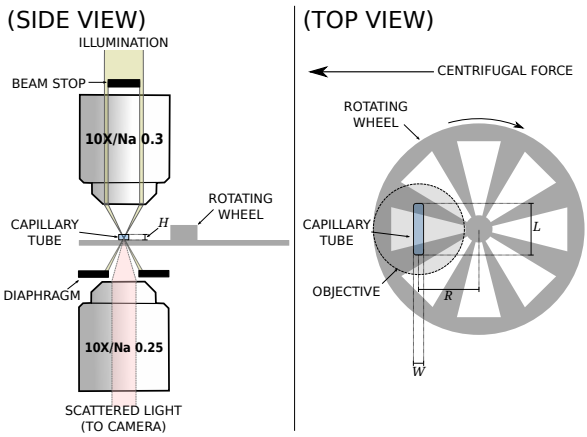

Figure 3.2: Experimental setup combining dark-field microscopy and a centrifugation apparatus. Left: in dark-field configuration a partially blocked illumination beam is focused onto the sample that scatters the incoming radiation. Illumination light is blocked and only scattered light is collected by the imaging objective. Right: the sample is contained in a capillary glass tube attached to a wheel driven by a precision motor.

microscopy. In the image acquired used bright field microscopy, the background is more noisy than in the one acquired using dark field microscopy. Furthermore, in dark-field image we mostly see only the bacteria in focal plane as bright spots. In the bright-field image, on the contrary, we see bacteria either in the focal plane as dark spots or bacteria above the focal plane as bright spots.

Large images (1800×1200 pixels, i.e. $\sim 0.65 \times 0.44$mm) are collected at a frame rate of 33 fps by a CMOS camera (Hamamatsu Orca Flash 2.8 [40]) for a total measurement time of about 60 s ($\sim$ 2000 images). The bacterial sample is contained in a rectangular capillary glass tube (Vitrocom) with internal dimensions of $1 \times 0.1 \times 10$ mm ($W \times H \times L$ in Fig. 3.2). Our images (~ 0.65 mm long) cover about one half of the capillary width W, which is aligned with the centrifugal force. The capillary tube is sealed with adhesive wax (VALAP [42], see also Sec.2.6.2), which is also used to fix the tube to the rotating wheel. The wheel is driven by a phase-locked loop motor spinnig the wheel up to 100 Hz. The glass tube is placed at a distance $R = 40$ mm from the center of the wheel.

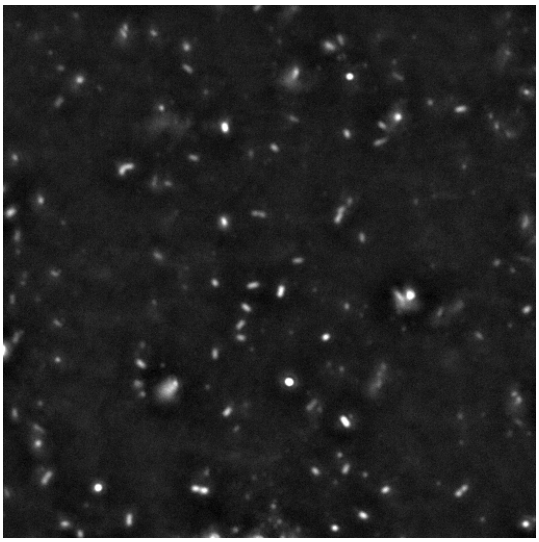

(a) Dark-field image

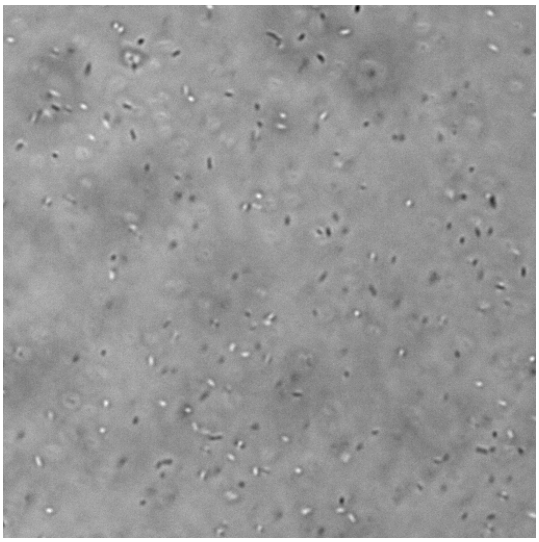

(b) Bright-field image

Figure 3.3: Comparison between dark-field (a) and bright-field (b) images of *E.coli* suspension. Images are acquired using a 20× objective.

Centrifugal acceleration

In Sec.1.4 we showed that natural sedimentation effects for microscopic objects are very slow in time. For this reason, we use centrifugation to enhance gravity and produce a more pronounced and faster sedimentation in the sample. We use typically centrifugation frequencies of about $\nu = 10$ Hz (600 rpm) corresponding to a centrifugal acceleration:

$$a = (2\pi\nu)^2 R \simeq 12g. \tag{3.2}$$

For $a \simeq 12g$ we estimate $v_d \simeq 1\,\mu$m/s. This sedimentation velocity is significant when compared with the typical swimming speeds of *E. coli* that are of order $\sim 10\ \mu$m/s. We tested also smaller centrifugal accelerations, $a = 7.7g, 4.3g$ (see Fig.3.9).

3.2.2 Bacteria samples

E. coli (MG1655) samples are prepared following the protocol described in Secs.2.3, 2.6.2.

3.2.3 Measurements

We start with a qualitative study of bacterial trajectories at low concentration. Images are acquired after centrifugation for 10 minutes at $a \simeq 12g$ and for a total time lapse of 6 seconds. We choose to focus on cells swimming close to the capillary interface where most trajectories are confined by the wall and stay within the field depth. As shown in Fig. 3.4, the non motile component is fully sedimented in a $\sim 50\mu$m thick pellet. Motile bacteria having a slow swimming speed appear as short trajectories, mostly confined near the bottom of the sample (left side in Fig. 3.4). By contrast, fast bacteria that trace longer paths are found throughout the whole sample. They are clearly seen in the right half of Fig. 3.4. Interestingly, the trajectories of fast bacteria are only rarely interrupted by sudden changes of direction (i.e. "tumbles"), signaling an average tumbling time longer than 6 seconds. To quantify these effects we performed ICS on more concentrated samples (10^9 cells/ml).
Image acquisition is performed *after* the centrifuge is stopped, i.e. while the swimming bacteria gradually start repopulating the whole sample. However, we can assume that, within the measurement time, the system is in a quasi-stationary state provided this re-diffusion process is much slower than the typical relaxation time.

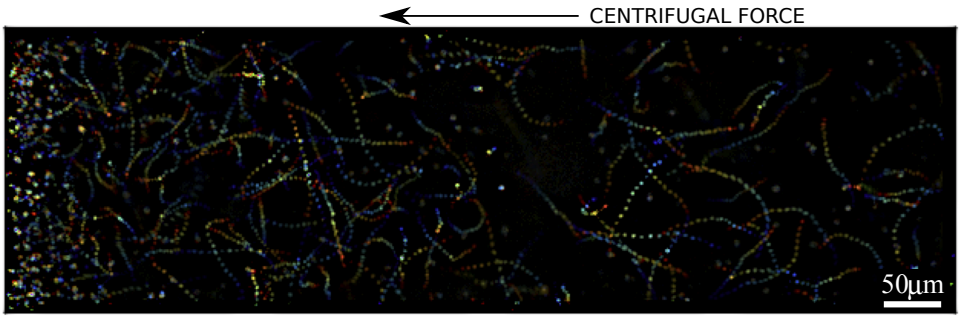

Figure 3.4: Traces of swimming bacteria after centrifugation at low bacterial density. Slow bacteria are found sedimented at the bottom of the sample (left side), while faster ones appear as the only visible component in the upper region of the sample(right side). Traces are obtained by superposing of frames progressively colored from red to blue as time increases.

(The stationarity approximation has been checked by subdividing the 60s-long image acquisition into six different 10s sub-measurement. From these sub-measurement we can obtain six different $g(\mathbf{q}, t)$, see Secs.2.5 and 3.3, which do not show any systematic change with the measuring starting time). Centrifugation could, in principle, induce some anisotropy in the bacteria motion by aligning bacteria along the field direction. However, we wait for several tenths of seconds after the centrifuge is stopped before taking our measurements. This ensures that bacteria have time to tumble and reorient substantially. This is also confirmed by looking at Fig. 3.4 where the trajectories appear randomized in all directions. In that situation we can assume that the motion of bacteria is isotropic.

3.3 Data analysis

The ICS method, described in Sec.2.5, links the image correlation function $g(q,t)$ with the intermediate scattering function allowing the calculation of motility parameters. In fact, $g(q,t) = A(q)\,F(q,t) + B(q)$ and for a bacteria suspension $F(q,t)$ can be modeled, see Sec.2.5.1, as

$$F(q,t) = e^{-q^2 Dt}\left[4\pi\alpha \int_0^\infty dv\, P(v)\,\mathrm{sinc}(qvt) + (1-\alpha)\right] \tag{3.3}$$

where e^{-q^2Dt} describes Brownian motion which bacteria are subject, α is the fraction of motile bacteria and $P(v)dv$ represent the probability of finding bacterium with speed between v and $v + dv$.

We model velocity distribution $P(v)$ as a superposition of hat functions [47]. This can be seen as a spline-interpolating curve approximating the actual $P(v)$. The resulting $P(v)$ is continuous, positive and bounded by some maximum speed $v_{\max}$ (i.e. $P(v > v_{\max}) = 0$). The spline $P(v)$ is thus written as

$$P(v) = \mathcal{N}^{-1} \sum_{j=1}^{M} c_j \, T_j(v) \tag{3.4}$$

where the $T_j(v)$ are the hat functions, each having amplitude c_j, and the sum is taken over the M functions used and the normalization factor $\mathcal{N} = \sum_{j=1}^{M} c_j \int dv \, T_j(v)$ ensures that $\int dv P(v) = 1$. We choose to set the first node at 1 μm/s so that the non-motile component is fully accounted by the $1 - \alpha$ term in Eq. (3.3). Following [47], we used 13 nodes spaced by approximately 5 μm/s. As a test, we check the effect on the $P(v)$ produced by changing the node spacing. To do this we change the total number of nodes between the first non-zero node at 1μm/s and $v_{max} = 60\mu$m/s, the range being kept fixed. This changes substantially the node density by a factor ranging from 0.5 to 2 (number of nodes ranging from 6 to 32). As may be seen on Fig.3.5 when the density of node is too low the spline $P(v)$ develops a spurious peak at high speed. Note also that fitting the same data with the standard Schulz distribution (the dashed line in Fig.3.5) gives a $P(v)$ whose peak is slightly shifted to the left. Varying the number of nodes from 13 to about 30 does not affect significantly the obtained fitted distributions (see Fig.3.5.) We can identify the velocity distribution $P(v)$ putting together Eqs. (2.12), (3.3) and (3.4) by a fitting procedure having as parameters $A(q)$, $B(q)$, D, α and the spline coefficients $c_j, j = 1, \cdots$. In principle, the fitting parameters D, α and c_j do not depend on q. In fact, they display minor variations in the range $0.4 \leq q \leq 1.15\,\mu\text{m}^{-1}$. Therefore, we choose to obtain $P(v)$ as an average over q values in that range. We expect that the presence of an acceleration field will lead to a space-inhomogeneous dynamics along the direction of centrifugal force. Therefore, we subdivide each image into seven sub-images (1200×256 pixels, i.e. $\sim 0.44 \times 0.093$ mm), as shown in Fig.3.6, and separately compute the image correlation function $g(q, t)$ for each of them. As a result, we obtain

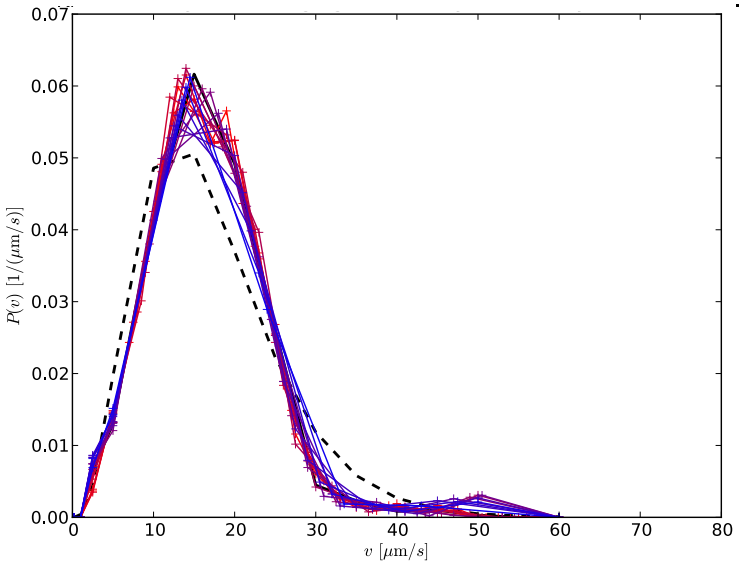

Figure 3.5: Fitted spline-probability distribution upon changing the node density with original density 0.22 nodes per μm/s (between 1μm/s and 60μm/s) by a factor ranging from 1/2 to 2 (blue to red). The dashed line is the probability obtained from a fit with the Schulz distribution. It is seen that when the nodes density is too low a spurious peak at high speed appears.

a set of seven intermediate scattering functions $F(q,t)$. We choose to focus on the high half of the sample, where we expect to find the fastest cells after centrifugation. In this configuration, the image ranges in height (following named z) from 0.95 mm and 0.39 mm.

In Fig. 3.7 we show the $F(q,t)$, for one single $q = 0.77\,\mu\text{m}^{-1}$, at two different heights before and after centrifugation. Fitted functions are represented by full lines. Fig. 3.7 shows quite clearly how the functions measured after a 10 min-long centrifugation at $a \simeq 12g$ relax faster than the functions measured in the unperturbed sample ($a = 0$). The two $F(q,t)$, measured at two different heights, in the unperturbed sample are very similar. Differently, in the centrifuged case we clearly see that the $F(q,t)$ measured at high z relaxes faster than the $F(q,t)$ measured at low z indicating that the average bacterial speed is higher at larger elevation. In

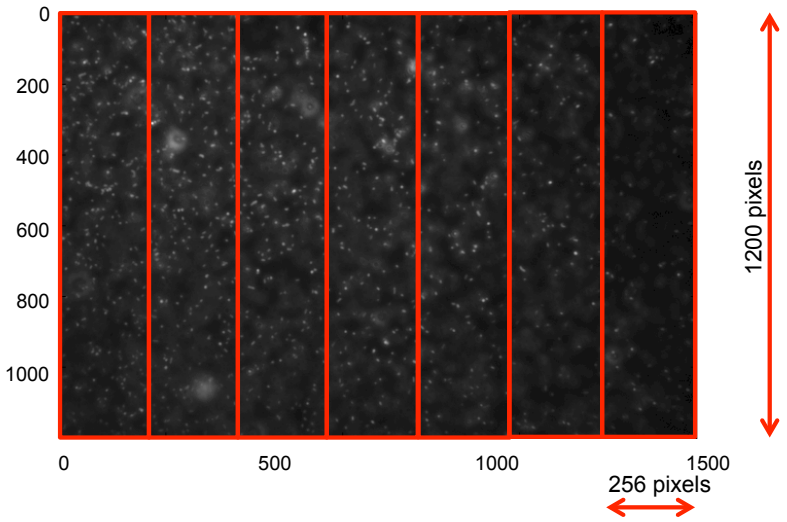

Figure 3.6: The acquired image subdivided into seven sub-images to study the effect of the centrifugal force.

addition, after centrifugation, the amplitude of the motile component increases from $\alpha \sim 0.3$ to $\alpha \sim 0.8$ at higher heights.

Throughout the range of centrifugations speeds and heights we always found diffusivities $D = 0.3 \pm 0.1\,\mu\mathrm{m}^2/\mathrm{s}$, which are consistent with the expected value for Brownian motion of non motile cells [39]. In Fig. 3.8 we plot the speed distributions before and after centrifugation. The original speed distribution of the unperturbed sample is denoted by $P_0(v)$. After centrifugation the speed distribution depends on height. This dependance is now explicitly introduced as a parameter in $P(v, z)$. In Fig.3.8 we show two speed distributions corresponding to the same two elevation values in Fig. 3.7. Note that the $P_0(v)$ shows a very high concentration of slow bacteria. Differently, $P(v, z)$ at $a = 12g$ is peaked around higher speeds demonstrating that centrifugation has sedimented most of the slow bacteria at low height. Note also that the $P(v, z = 0.95)$ is shifted to higher speeds compared to the $P(v, z = 0.39)$. Interestingly, the $P(v, z = 0.39)$ is quite similar to a Shultz distribution [37, 39], while at 0.95 mm we find a less biased $P(v, z)$. From $P(v, z)$ we can determine the

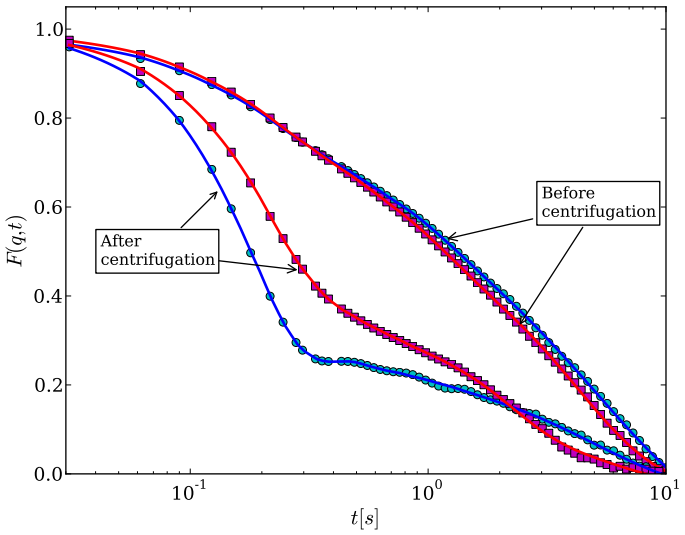

Figure 3.7: Intermediate scattering functions ($q = 0.77\,\mu\mathrm{m}^{-1}$) obtained from ICS, before and after centrifugation, at 0.39 mm (solid squares □) and 0.95mm (hollow circles ○). The two faster relaxing $F(q,t)$ are measured after a 10 min-long centrifugation at $a \simeq 12g$. Full lines are fit with the model function in Eq. (3.3). Note that in the $a = 12\,g$ case the $F(q,t)$ relaxes faster at 0.95 mm than at 0.39 mm, indicating that the average speed of bacteria is higher at larger heights.

average speed $\langle v(z)\rangle = \int dv\, P(v,z)\, v$. The $\langle v(z)\rangle$, corresponding to the measurement in Fig. 3.4 and 3.7, is shown in Fig. 3.9(a) for all heights between 0.36 and 0.95 mm. $\langle v(z)\rangle$ grows from about 13 μm/s to almost 17 μm/s as z increases. In Fig. 3.9(b) and (c) we also show the effect of reducing the centrifugal acceleration applying centrifugation to two additional samples prepared from the same (not centrifuged) original sample. The $\langle v(z)\rangle$ in Fig. 3.9(b) and (c) were measured after 10 min-long centrifugation with $a \simeq 7.7\,g$ and $4.3\,g$ respectively. It can be seen that the whole $\langle v(z)\rangle$ profile shifts to lower speeds upon decreasing centrifugal acceleration. In addition to the average speed we can study the behavior of the standard deviation of the speed $\sigma(z)$, given by $\sigma(z)^2 = \int dv\, P(v,z)\,(v - \langle v(z)\rangle)^2$. The $\sigma(z)$, corresponding to the measurement in Fig. 3.4 and 3.7, is shown in Fig. 3.9(a) as a function of z. It can be seen that $\sigma(z)$ has a much weaker dependence on z com-

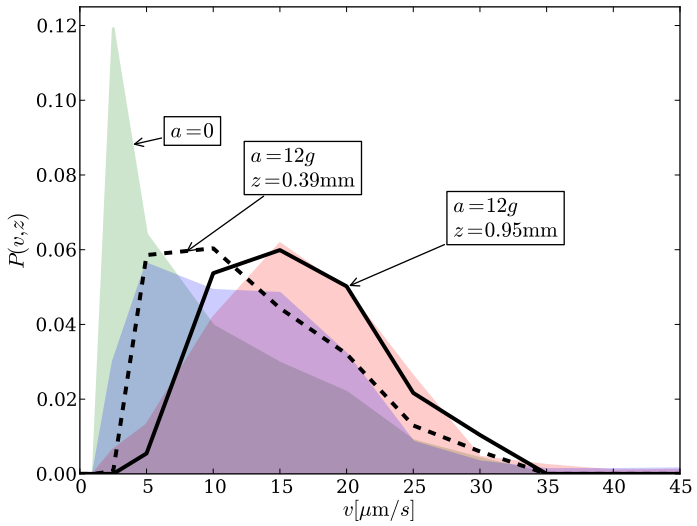

Figure 3.8: Speed probability density functions measured in the non centrifuged ($a = 0$) and the centrifuged sample ($a = 12g$) represented by the colored areas. The $P(v, z)$ of the centrifuged sample is displayed at two heights, $z = 0.95\,\text{mm}$ and $z = 0.39\,\text{mm}$ (as indicated by the arrows) obtained from the fits of the two $F(q, t)$ of Fig. 3.7. Note that the $P(v, z)$ shifts to higher speed and changes shape at higher heights. The dashed and the solid line are, respectively, the $P(v, z)$ at 0.36 mm and at 0.95mm, obtained from the $P_0(v)$ of the non centrifuged sample, using the model presented in Sec. 3.4.

pared to $\langle v(z)\rangle$. $\sigma(z)$ decreases only of about 1μm/s upon increasing z. This is also evident from Fig. 3.8, where one can see that the $P(v, z)$ shifts to higher speeds and changes shape as z increases but its width remains quite large. Moreover $\sigma(z)$ weakly increases while the centrifugal acceleration decreases as shown in Fig. 3.9(b) and (c). We also check the effects of centrifugal acceleration on the fraction of motile cells α. Fig.3.10 shows α values at $a \simeq 12\,g$, $7.7\,g$ and $4.3\,g$. The increase of α after a centrifugal force is applied is due to the increase of the average speed (see Fig.3.9). Similar to $\langle v(z)\rangle$, the whole α profile shifts to lower values for smaller centrifugal acceleration. In the case of *E. coli* bacteria, careful procedures have been developed to start off with a suspension of cells having high motility characteristics. Typical

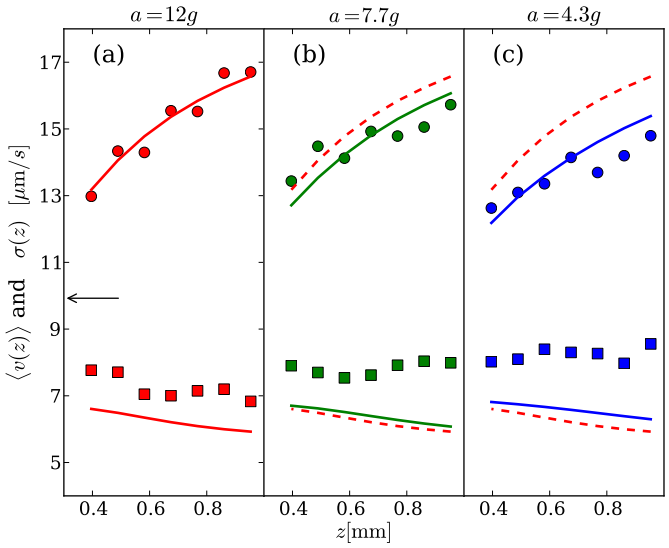

Figure 3.9: (**a**) Average speed $\langle v(z)\rangle$ (solid circle ●) and standard deviation $\sigma(z)$ (solid squares ■) as function of z after centrifugation at $a \simeq 12\,g$, corresponding to the same measurement of Figs. 3.7, 3.8. The arrow point to the mean speed (solid line) of the non centrifuged sample. Note how $\langle v(z)\rangle$ increases for increasing z. The solid line is obtained by a heterogeneous diffusion model, discussed in Sec. 3.4. (**b**) and (**c**) $\langle v(z)\rangle$ (●) and $\sigma(z)$ (■) as a function of z after centrifugation at $a \simeq 7.7\,g$ and $4.3\,g$ respectively. The full line in (a) is reproduced in (b) and (c) as a dashed line for an easier comparison. This shows how the $\langle v(z)\rangle$ shifts to lower speeds for decreasing a.

speed distributions [39] compare well with what we observe in the small z fraction of the centrifuged sample with a relative width ($\sigma/\langle v\rangle$) of 0.6. The high z component of the centrifuged sample further improves motility, leading to a distribution having a higher average and a smaller relative width 0.4. In principle, as will be discussed in the following section, our method works for any kind of self propelled objects and could be particularly useful in the case of biological or chemical swimmers that can only be produced with highly polydisperse speeds.

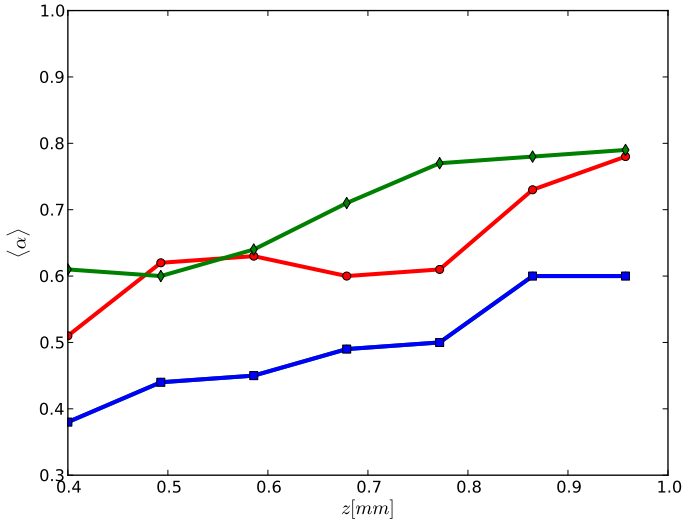

Figure 3.10: Averaged α values after centrifugation at $a \simeq 12\,g$ (red line with circles), $a \simeq 7.7\,g$ (green line with diamonds) and $a \simeq 4.3\,g$ (blue line with squares).

3.4 Modeling

In Sec.1.4 the behavior of swimming cells under the action of an external field was modeled. The run-and-tumble motion of bacteria subjected to an external field leads to a probability of finding a cell in a given position in space different with respect to non motile particle. In our experiment, a centrifugal acceleration a directed along the z-axis adds a drift-speed component $v_d\hat{\mathbf{z}}$ to the velocity $\mathbf{v}$ of the cell. If the external field is applied for a sufficiently long time, the population of swimming cells will attain a stationary density profile. In this situation, the probability $\rho(z,v)dz$ of finding a bacterium with speed v in the range $(z, z+dz)$ decays exponentially with z [4]:

$$\rho(z,v) = \mathcal{N}^{-1}\exp(-\kappa\, z). \tag{3.5}$$

The dependence on v is through the sedimentation rate κ, $\mathcal{N} = \int_0^H \exp(-\kappa\, z)$ is a normalization constant obtained by integrating over the whole sample of height H. The actual value of κ depends on the bacteria speed, their tumbling rate and the

drift speed, according to the transcendental equation [4]:

$$\ln\left[\frac{\kappa(v+v_d)+\lambda}{\kappa(v-v_d)+\lambda}\right]=\frac{2\kappa v}{\lambda} \tag{3.6}$$

In Sec.1.4 it is shown that, in the limit of small v_d, $\kappa = v_d/D_{\rm eff}(v)$ where $D_{\rm eff}(v) = v^2/(3\lambda)$ is the effective diffusion coefficient for a run-and-tumble dynamics and λ is the tumble rate. In this case, Eq.(3.5) takes the Boltzmann form in Eq.(3.1) with an effective diffusion coefficient $D_{\rm eff}(v)$:

$$\rho(z,v)=\mathcal{N}^{-1}\exp\left(-\frac{v_d}{D_{\rm eff}(v)}\,z\right)=\mathcal{N}^{-1}\exp\left(-3\frac{v_d\lambda}{v^2}z\right) \tag{3.7}$$

We have checked numerically that the approximation provided by Eq.(3.7) gives practically the same results of Eq.(3.5) in the range of present interest and for the drift speeds ($\sim 1\mu$m/s) prevailing in our experiment. Fig.3.11 illustrates the behavior

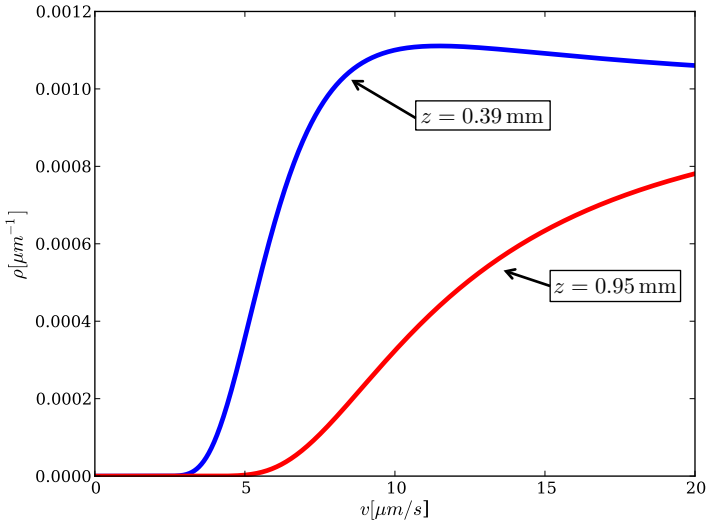

Figure 3.11: Bacterial density $\rho(z,v)$ as a function of v at $z = 0.95$mm and $z = 0.39$mm.

of $\rho(z,v)$ (Eq. (3.7)) at the maximum and minimum experimental heights, having chosen as parameters $v_d = 0.45\,\mu$m/s and $\lambda = 0.1$Hz (values compatible with the

fitting parameter γ shown below). To quantitatively account for the distribution of speeds in the bacteria population we consider the probability density function of the speed $P_0(v)$ for null external field. As mentioned in the previous section this function is measured experimentally in the non centrifuged sample. When the centrifugal field is applied, the probability of finding a bacterium with speed within $(v, v + dv)$ and located between z and $z + dz$ is given by $P_0(v)\,\rho(z, v)\,dv\,dz$. From this expression we see that the function $\rho(z, v)$ acts as a filter that reduces the probability of finding slow bacteria in the high-z regions (see Fig.3.11).Therefore, the z-dependent speed distribution is given by

$$P(v, z) = \mathcal{N}^{-1} P_0(v)\,\rho(z, v) \tag{3.8}$$

where $\mathcal{N} = \int dv\, P_0(v)\,\rho(z, v)$. Since v_d and λ are multiplied in Eq.(3.7) we choose $\gamma = \lambda v_d$ as the only free fitting parameter. To find γ we fit the average speeds at different elevation measured after centrifugation at $a = 12g$ with the function $\langle v(z)\rangle = \int \mathcal{N}^{-1} P_0(v) v\,\rho(z, v)$. This fit is represented by the solid line in Fig. 3.9(a) giving the best-fit parameter $\gamma = 4.5 \times 10^{-2}\mu\text{m/s}^2$. This value of γ is compatible, for example, with the values $v_d = 0.45\,\mu\text{m/s}$ and $\lambda = 0.1$ Hz. This v_d is of the same order of magnitude of the estimate given before and this tumbling rate λ is consistent with that obtained by direct imaging of bacteria trajectories, discussed at the beginning of Sec. 3.2.3. Recall that the traces of bacteria displayed in Fig. 3.4 show that cells swim along roughly straight runs for about 6 s without evident signs of tumbling. The observed value for the tumbling rate is about one order of magnitude smaller than that generally reported in the literature [2]. It will be important to investigate the presence of a heterogeneous tumbling frequency among our cells and the possible role of centrifugation in selecting the smoothest swimmers. In Fig. 3.8, we show the $P(v, z)$ at $z = 0.95\,\text{mm}$ (full line) and the $P(v, z)$ at $z = 0.36\,\text{mm}$ (dashed line) obtained from Eqs. (3.7) and (3.8) using the fitted parameter $\gamma = 4.5 \times 10^{-2}\mu\text{m/s}^2$. Note that the modeled $P(v, z)$ follows quite well the corresponding measured function. When computing $\sigma(z)$ we also find a slightly decreasing trend for increasing z, while experimental values are systematically higher (see Fig. 3.9(a)). The model predicts that the $\sigma(z)$ should decrease upon increasing z and the data seem to follow this trend. To further test the model, we have

computed the quantities of interest at different centrifugal accelerations. Since the drift speed, and hence γ, are proportional to the centrifugal acceleration ($v_d \propto a$) we can obtain the $P(v, z)$ at different values of a by simply rescaling γ. The $\langle v(z) \rangle$ obtained in this way are represented by full lines in Fig. 3.9 (b) and (c) for the centrifugal accelerations $a = 7.7\,g$ and $4.3\,g$ respectively. Now, the model has no fitting parameters it shows an overall decrease of $\langle v(z) \rangle$ with decreasing a, which is in quantitative agreement with the data shown Fig. 3.9 (b) and (c). When the parameter γ is let free in the fitting procedure, this is found to be approximately the same at all centrifugal accelerations ($\gamma \approx 4 - 5 \times 10^{-2} \mu\mathrm{m/s}^2$). With the same calculation, we can estimate $\sigma(z)$ at $a = 7.7\,g$ and $4.3\,g$. Theoretical values are represented by the solid lines in the lower part of Fig. 3.9 (b) and (c). They are still systematically smaller than the measured ones. This could be due to an intrinsic fluctuation of swimming speeds of individual cells.

3.5 Conclusions

By applying a centrifugal field on an *E. coli* suspension, we have demonstrated that centrifugation has significant effects on the spatial distribution of motility. By using dynamic image correlation spectroscopy, we have found that a substantial speed gradient is produced in the direction of the centrifugal acceleration. Finally, we have compared our results with a theoretical model describing bacteria as particles with an effective diffusion. This model shows that bacteria can be described as "hot colloids" with an effective diffusion coefficient depending on their speed. When compared to other strategies for motility sorting, such as those based on microfabrication, centrifugation offers several important advantages, such as easy tunability, large sample volumes, fast operation and easy implementation. Our findings could be further used to design novel microfluidic procedures aiming at sorting out highly motile cells from a heterogeneous population. This would be important both for micro-engineering applications exploiting self-propulsion and for further investigation of the biological factors associated with high motility.

Chapter 4

E.coli in an asymmetric landscape: colloidal delivery

4.1 Introduction

In this chapter we show that it is possible to design three dimensional structures in which passive colloidal particles can be spatially organized by a suspension of swimming bacteria [9].

Colloidal particles exhibit a Brownian motion due to stochastic and rapid collisions with solvent molecules. This diffusive motion leads to a uniform density distribution in the space available if the external field is null. Concentrating particles in a specified area requires an external field to do work in order to make the target configuration energetically favorable. Boltzmann's distribution, in fact, predicts that the equilibrium density of non-interacting particles is a local function of energy density alone, independent of particle trajectories. On the contrary, active particles, such as swimming bacteria or chemically propelled colloids, are driven by a non-equilibrium stochastic force, which may typically be characterized by a persistence time of the order of a few seconds [2, 3]. The possibility to rectify an out-of-equilibrium dynamics by means of an asymmetric environment was described in Sec.1.6, where it was shown that the interaction with a wall of funnels leads to a different concentration of bacteria on the two sides of the wall. Bacteria are also able to produce an

unidirectional rotation of an asymmetric gear via a cooperative motion [6, 7]. Also passive colloidal particles, put in an active bacterial bath, display a random walk with a finite persistence length [48, 49, 50]. This observation led us to hypothesize that also this out-of-equilibrium dynamics could be rectified by using an asymmetric landscape. Bacteria have already been used as micro-propellers to deliver colloids by joining them onto the surface of micro-cargos [51, 52, 53]. However, an external signaling system has to provide the stimuli needed to guide and release the bacterial cargo [52, 54, 55]. In our experiment, we observed that bacteria are able to drive colloids, initially uniformly distributed, into a target area of about $16 \times 16\mu\text{m}^2$. To achieve this results we used a microfabricated 3D structure without use external control field or attaching bacteria on colloid cargo .

4.2 Experiment

4.2.1 Basic principle and implementation

In this experiment, we explore the colloidal behavior in a bacterial bath embedded in an asymmetric landscape made of microfabricated structures. The basic principle in our method is illustrated in Fig.4.1.

We start by describing the simpler situation in which only non-interacting Brownian particles are considered. Let us suppose that beads can hop between two metastable states, 0 and 1, with the same energy and the same spatial extent δ. In equilibrium, the number of particles n_0 in 0 is equal to n_1 particles in 1, independently of the shape of the barrier. The situation may change drastically if we add a fluctuating noise with a finite correlation time. If the force persistence time is larger than the transition time, the probability to jump from a state to the other depends on the probability of being pushed by the bath with a force of amplitude ξ larger than the slop of the energy barrier f_0. Considering that in general a small ξ will be more frequent than a larger ξ, the most probable transition will be the one with a minor slope, i.e. from 1 to 0. This results in a biased transition rate between the two states, producing a stationary state in which particles spend more time in state 0 than in state 1. Defining λ_{01} and λ_{01} the transition rate from 0 to 1 and from 1 to

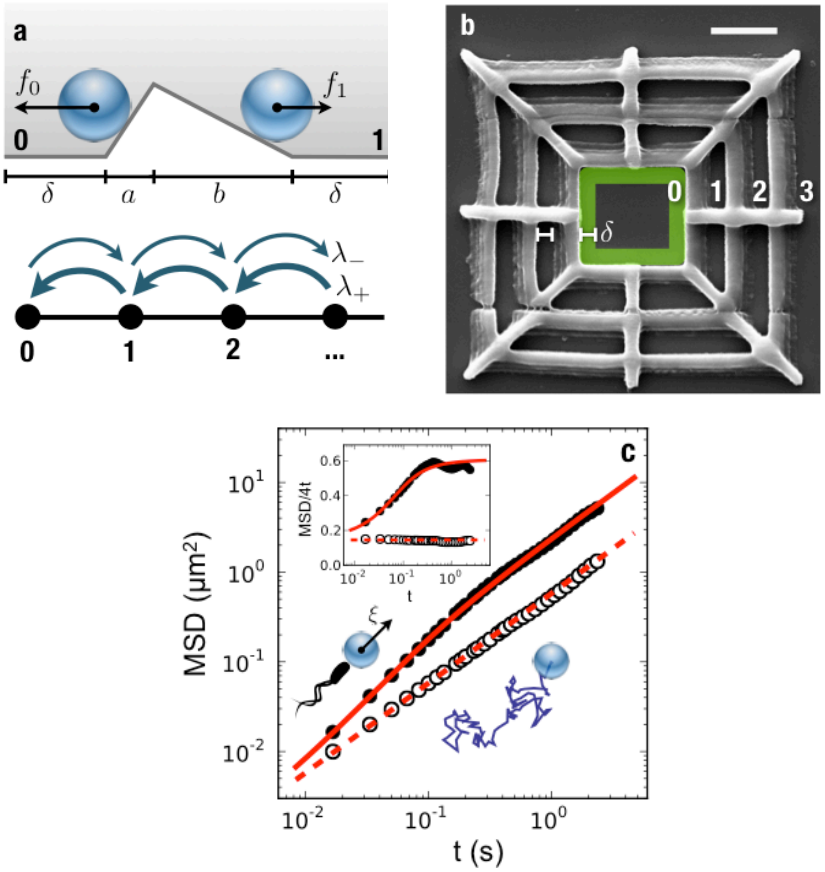

Figure 4.1: Basic principle and experimental setup. (a) A schematic representation of the main geometric and dynamical features of transitions between states separated by asymmetric barriers. (b) A scanning electron microscopy image of a square structure that gathers particles in the central chamber. Radial walls enhance structural stability. Scale bar, 10 μm in length. (c) The mean squared displacements (MSD) of the beads in the absence of bacteria (simple Brownian motion, hollow circles) and in the bacterial bath (solid circles). Solid and dashed lines, fitted to the data, give a persistence time of $\tau_c = 0.04\,\mathrm{s}$ for the active system. The inset depicts the same data as an effective diffusivity (computed dividing the MSD by 4τ), clearly showing the super diffusive regime at short times. The Brownian diffusivity is $D_0 = 0.15\mu\mathrm{m}^2\mathrm{s}^{-1}$, whereas after adding bacteria we measure an additional active term $D_A = 0.45\mu\mathrm{m}^2\mathrm{s}^{-1}$.

0, the stationarity condition will be:

$$n_0\lambda_{01} = n_1\lambda_{10} \rightarrow n_0 = \frac{\lambda_{10}}{\lambda_{01}}n_1 \tag{4.1}$$

In more complex situations, where a 2D region is surrounded by a series of sequential barriers $0, 1, 2, \ldots$ with asymmetric walls as in Fig.4.1(a), the transitions rates are :

$$\lambda_{01} \sim \lambda_{12} \sim \lambda_- < \lambda_{10} \sim \lambda_{21} \sim \lambda_+ \tag{4.2}$$

In the inner region 0 the number of particles can increase by a factor $(\lambda_+/\lambda_-)^m$ where m is the number of barriers. If $(\lambda_+/\lambda_-) \simeq 2$ three barriers are enough to lead to an increase in the particles density of about an order of magnitude. We designed a 3D structure, shown in Fig.4.1(b), implementing a 2D pattern of energy barriers over a flat surface. The gravitational force acting on beads transforms the wall geometry into an asymmetric energy landscape. To drive colloidal beads with an out-of-equilibrium stochastic force we use motile bacteria.
We check the difference between the mean square displacement (MSD) of beads in a absence of bacteria and in a bacterial bath. As shown in Fig.4.1(c), the active system has a persistence time of $\tau_c = 0.04\,\mathrm{s}$. Moreover, the active system displays a super-diffusive behavior at short times, see inset in Fig.4.1(c).

4.2.2 Bacteria samples

E.coli(MG1655) samples are prepared according to the protocol described in Secs.2.3 and 2.6.2. To perform this experiment, salt was removed from the recipe of the growth medium and of the motility buffer, to avoid that particle aggregate and stick to the cover glass. We have not observed any significant change in the growth and motility characteristics of our bacteria in the salt-free medium. In fact, the bacteria growth rate without salt does not show a significant deviation from the growth rate of a usual *E.coli* sample (see Fig.4.2). Furthermore, as pointed out in Sec.2.3, a motility buffer without salt still have a pH(~ 7) suited to motility.

4.2.3 Microfabrication

Microfabrication is performed by a holographic optical tweezer setup [13, 56]. A reflective liquid crystal SLM (Holoeye LC-2500) is employed to impose a computer-

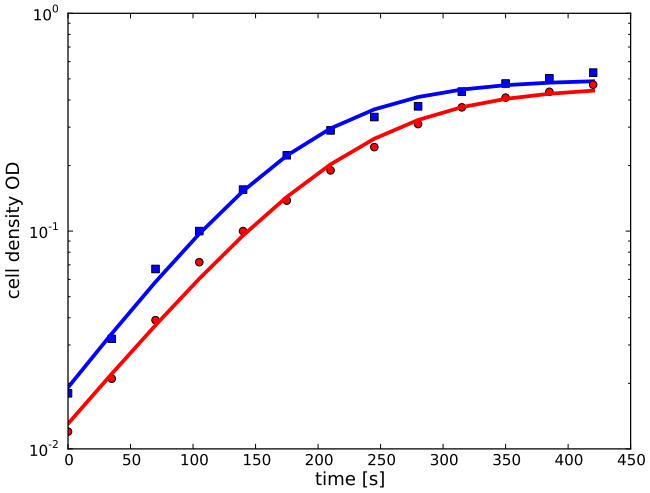

Figure 4.2: Growth curves of *E.coli* with and without salt: blue squares (□) represent the measured Optical Density of *E.coli* sample growing in standard condition described in Sec.2.3, red circles (○) represent the measured O.D. density of *E.coli* growth without any salt. Dashed lines are fitted to the data. The two different conditions do not modify significantly the growth rate, from the fit: $\tau_{standard} = 40 \pm 2$min and $\tau_{noSalt} = 44 \pm 1$min

generated pattern of phase shifts generated by CUDA parallel processing onto an expanded laser beam (DPSS Opus Ventus 532 nm, 3 W)[57, 58]. The emerging wavefront is focused by a large numerical aperture microscope objective (Nikon Plan Apo VC 100, numerical aperture= 1.4) onto an array of spots as determined by the parameters of the structure being built. We used Norland NOA 63, as a patterning photopolymer, an ultraviolet curing adhesive. Although the adhesive sensitivity lies outside the laser wavelength, the low absorption allows for intensity-based threshold processing. After fabrication, the uncrosslinked glue is removed by gently washing with toluene and then drying out in open air.

SEM images of the microstructure are shown in Figs.4.1(b) and 4.3(c). The device is composed of three concentric square barriers having a steeper slope pointing on the inner side (swapping the sides we built a structure that is expected to eject beads). Figs.4.3(a) and (b) represented a 3D sketch of both structures. The structure has a height of about 2μm, a side slope with horizontal distance $a \simeq 0.5\,\mu$m and $b = 2\,\mu$m (see Fig. 4.1(a)).

4.2.4 Sample preparation

A surfactant solution of 1% Tween 20 is applied on the glass coverslips, let to dry and placed in a microscope coverslip holder. Silica beads of $2\,\mu$m diameter (Bangs Laboratories Inc.) are dispersed in the bacterial motility buffer. A colloidal solution (2.5 μl) is added to the coverslip surface, followed by a $2.5\,\mu$l of bacterial solution, resulting in a sample height of about 150 μl. The holder is then sealed. Humidity throughout the experiment is maintained with a damp cloth. Fig.4.4 shows a sketch of the sample holder.

4.2.5 Particle imaging

Images are acquired with 20× and 40× Nikon Plan Fluor objectives in a bright-field microscopy setup. Particle tracking is accomplished through a centre of mass algorithm after subtracting the average background and filtering with a threshold. Particle numbers in different structures are initially computed by tracking and then verified by observation and counting. In order to extract the persistence time and diffusivities, the 2D mean squared displacements are fitted by a simplified active

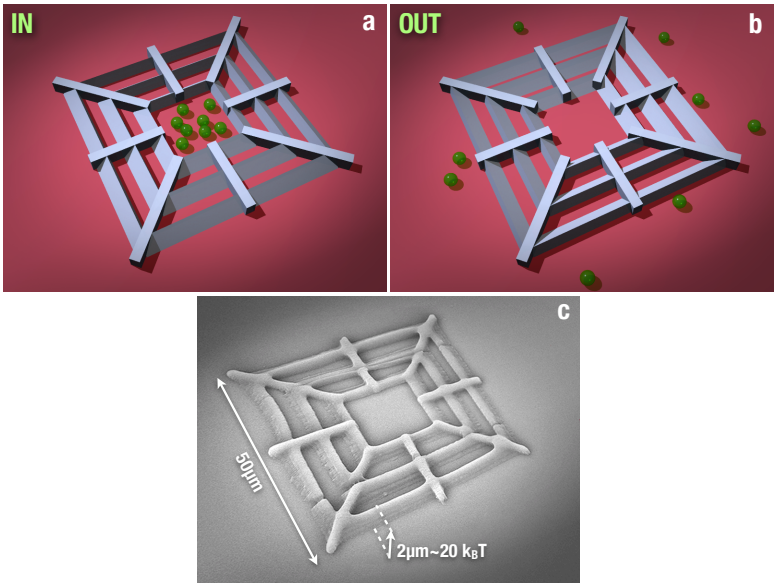

Figure 4.3: Panels a and b show 3D renderings of the original design of the gathering and scattering structures. Panel c shows the post-processed perspective SEM image of a fabricated gathering structure.

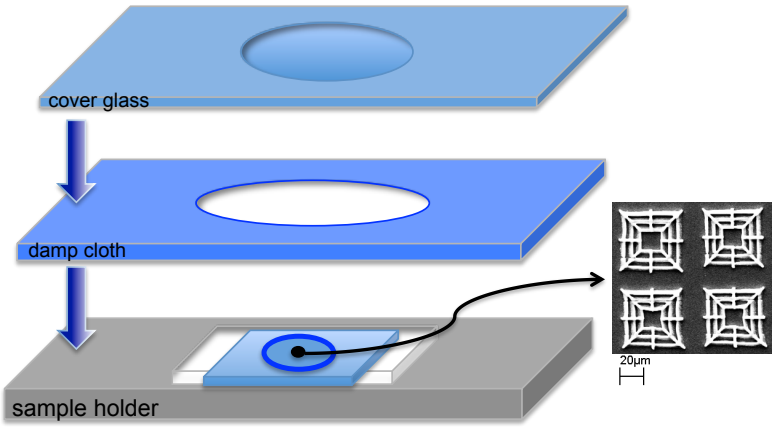

Figure 4.4: Schematic of the sample preparation: the micro-structure is fabricated on a coverslip placed in a sample holder. After putting the colloidal and bacterial solutions on the coverslip, the sample is closed with a damp cloth covered by a microscope slide. A SEM image of the microstructure is given on the right. Scale bar, 20 μm long.

diffusion model [50] with an extra short time Brownian diffusive term:

$$\langle \Delta r^2 \rangle = 4D_{\mathrm{A}}[\tau - \tau_{\mathrm{c}}(1 - e^{-\tau/\tau_{\mathrm{c}}})] + 4D_0\tau \tag{4.3}$$

with τ_{c} the correlation time, D_{A} the long time active diffusivity and D_0 the Brownian diffusivity.

4.3 Results

4.3.1 Observation of colloidal accumulation and depletion operated by bacteria

Our experiment is illustrated in Fig.4.5. Beads, in green, are digitally tracked on a surface with gathering and scattering structures. At the beginning, after all beads are sedimented we have a surface number density that, by direct counting, we find to be ρ_{c}=0.013 $\mu\mathrm{m}^{-2}$. We set time $t = 0$ soon after the introduction of bacteria, while the distribution of beads is still homogeneous and the concentration of cells is uniform. The surface number density of bacteria is ρ_{b}=0.014 $\mu\mathrm{m}^{-2}$. After about twenty minutes, the gathering structures are filled up, while scattering one are depleted (Fig.4.5b). A time-averaged bead positions during the last 5 minutes of the run, Fig. 4.5c, shows marked accumulation and depletion. Without bacteria however, colloidal particles, driven solely by thermal fluctuations, remain trapped in the structures' compartments, Fig.4.5d. In fact, a bead cannot jump over the barriers, since its thermal sedimentation length is 0.1 μm corresponding to an energy barrier of about 20 $\mathrm{k_B T}$. Boltzmann statistics would predict a uniform probability density throughout the flat regions in our system, corresponding to the same energy level. A colloidal density of ρ_{c}=0.013 $\mu\mathrm{m}^{-2}$ corresponds to an average of 3.3 particles in the inner chamber of the gathering structures. Without bacteria, the gathering structures at the top left and bottom right of Fig.4.5d contain respectively 2 and 7 particles. Assuming a Poisson probability distribution, those configurations are expected to occur with probabilities of 20% and 3%, respectively. On the contrary, after the addition of bacteria, the same two structures contain an average of 13 particles over the last 40 seconds (see Fig.4.6). This would only occur with a probability 0.003%, assuming a uniform density distribution as in equilibrium.

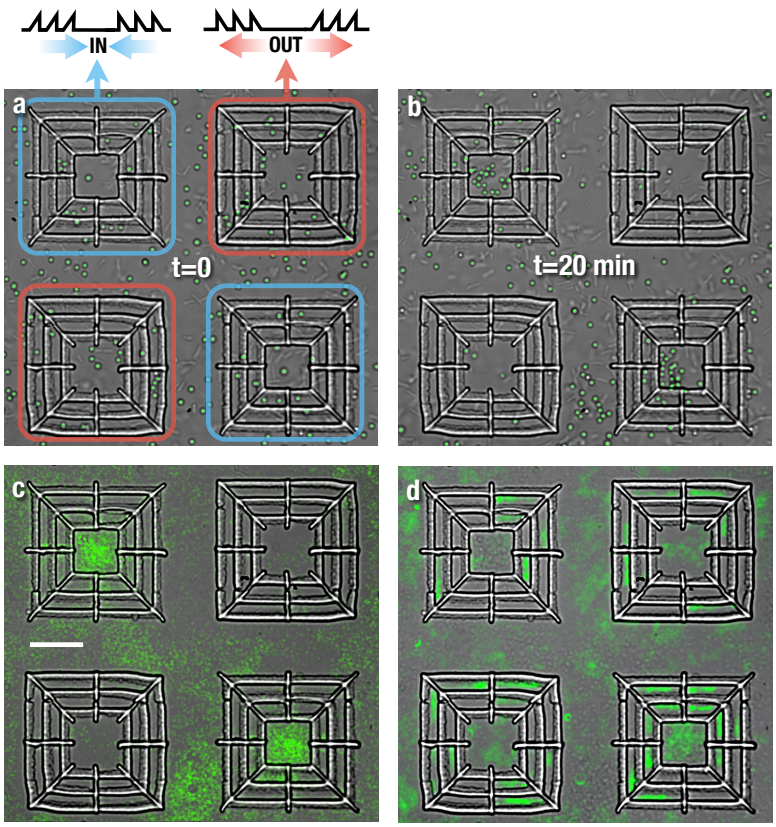

Figure 4.5: Observation of particle concentration and depletion operated by bacteria. Single experiment snapshots of particles and bacteria at the initial time ($t = 0$) where particles are randomly distributed (panel **a**) and for $t = 20$ min, where particle distributions have been strongly affected by bacterial transport over asymmetric barriers (panel **b**). Colloidal particles that are not stuck on the surface are highlighted in green. Particle distributions averaged over a steady state are shown in panel **c** for particles in the bacterial bath between $t_1 = 15$ min and $t_2 = 20$ min ($\Delta t = 5$ min) and in panel **d** for particles in an experiment without bacteria, undergoing simple Brownian motion for $\Delta t = 10$ min. Without bacteria, colloidal particles remain trapped within the structures compartments. The scale bar in panel **c** is 20 μm long.

4.3.2 Time evolution and transition rate modeling

In order to get a quantitative estimate of the transition rates we have recorded the time evolution of the number of beads in the three internal areas of all structures. Averaged data, corresponding to the gathering and scattering structures in Fig. 4.5, are reported in Fig. 4.6. As preliminary model, we assume that the number of beads in each region is governed by a coupled set of linear rate equations. Calling $\mathbf{N} = (n_0, n_1, n_2)$ the array of particle numbers we have:

$$\dot{\mathbf{N}}(t) = -\mathbf{\Lambda}\mathbf{N}(t) + \mathbf{S} \tag{4.4}$$

with $\mathbf{\Lambda}$ the rate matrix:

$$\mathbf{\Lambda} = \begin{pmatrix} \lambda_{01} & -\lambda_{10} & 0 \\ -\lambda_{01} & \lambda_{10} + \lambda_{12} & -\lambda_{21} \\ 0 & -\lambda_{12} & \lambda_{21} + \lambda_{23} \end{pmatrix} \tag{4.5}$$

and $\mathbf{S} = (0, 0, s)$ a source term, where s is the probability per unit time that a bead enters from outside. Since in the states 1 and 2 the beads are confined to be within the same distance δ from the two walls, it is reasonable to assume that $\lambda_{12} = \lambda_{23} = \lambda_{\text{out}}$ and $\lambda_{21} = \lambda_{10} = \lambda_{\text{in}}$. However, we can expect that λ_{01} is significantly lower than λ_{12}, since beads in 0 are on average at a larger distance from the wall. We account for this effect by assuming $\lambda_{01} = \alpha\lambda_{\text{out}}$, with $\alpha < 1$ being the probability for a bead in region 0 to be located within a distance from the wall equal to δ. We estimate α as the ratio between the shaded area in Fig. 4.1b and the total area of region 0. With reference to Fig. 4.1a, the values of λ_{in} and λ_{out} will correspond respectively to λ_+ and λ_- for the gathering structures and to λ_- and λ_+ for the scattering ones. The formal solution of (4.4) reads:

$$\mathbf{N}(t) = e^{-\mathbf{\Lambda}t}[\mathbf{N}(0) - \mathbf{N}(\infty)] + \mathbf{N}(\infty) \tag{4.6}$$

with the stationary state $\mathbf{N}(\infty) = \mathbf{\Lambda}^{-1}\mathbf{S}$. Defining $\overline{n}$ as the constant average number of beads that lay within a distance δ from the outer wall, we can write $s = \overline{n}\lambda_{\text{in}}$ and have $n_0(\infty) = \alpha(\lambda_{\text{in}}/\lambda_{\text{out}})^3\overline{n}$. This model completely neglects the excluded volume interactions between particles, that will set a maximum number of beads that a structure can accommodate in its interior. Nevertheless, we find a single set of fit-

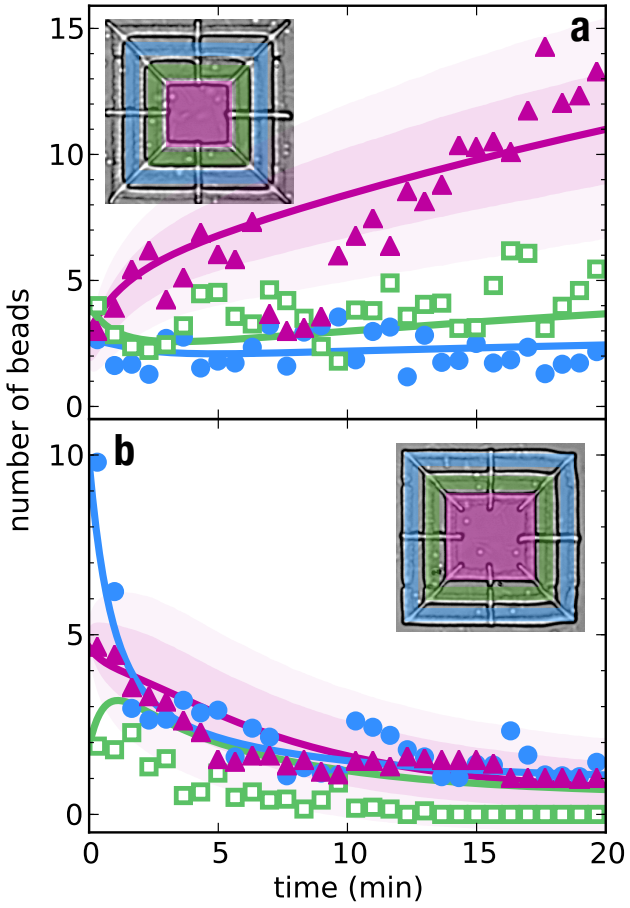

Figure 4.6: Temporal evolution of particle numbers within structural compartments. Particle numbers from a single experiment are averaged between the two gathering (**a**) and scattering (**b**) structures shown in Fig. 4.5. Each structure is subdivided into three compartments as highlighted by shaded areas in the insets: center (purple, triangles), middle (green, squares) and outer (blue, circles). Solid lines represent the best fit solution to the rate equation (4.6). Shaded areas in the plot represent the expected one and two standard deviation limits for predicted fluctuations in the evolution of beads numbers.

ting parameters λ_+, λ_- and $\overline{n}$ that describes well the observed filling and emptying processes on both structures (Fig. 4.6). In particular, we obtain $\lambda_+ = 0.66$ min^{-1} and $\lambda_- = 0.36$ min^{-1} with a ratio λ_+/λ_- equal approximately to 2. The fitted value

of $\overline{n}$ is 1.8, which is of the order of the average number of particles laying within a distance δ from the outer boundary of the structure. The fitted curves are drawn as solid lines in Fig. 4.6. In addition, for the innermost chambers, we report also the expected one and two standard deviation limits for fluctuations. While data for scattering structures seem to show a reasonable noise level, the number of particles in the center of gathering structures shows extremely large fluctuations. We conjecture that these fluctuations arise from collective effects neglected in our simplistic analysis, but likely important once colloidal beads start to pack together. However, accumulation effects over multiple and independent experiments are systematic and reproducible, as shown in Fig. 4.9.

4.3.3 Role of bacteria concentration

It is expected that the jump rates and steady state probabilities depend on many parameters, the most obvious of which are the height and slopes of the structures. Other parameters include particle size and density, the bacterial concentration and motility. In particular, we find that when the bacterial density is increased, beads

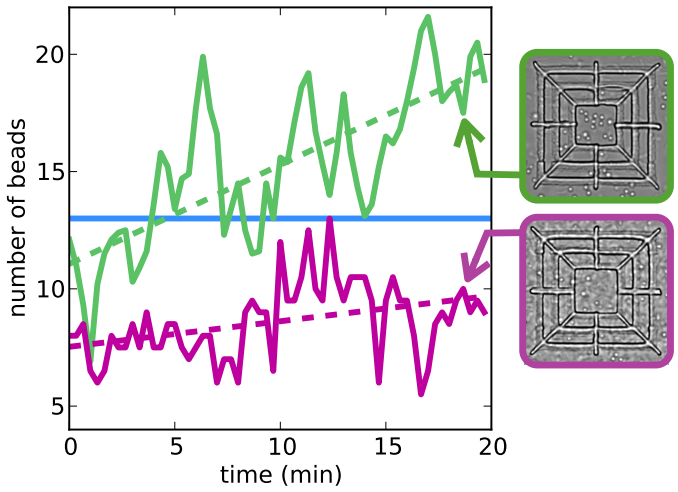

Figure 4.7: Effect of the bacterial density on filling efficiency. Solid lines represent the time evolution of total beads count over entire filling structures in the case of low and high bacteria densities: ρ_b =0.014 (green) and 0.2 (purple) μm^{-2}. The horizontal blue line shows the unchanging particle number in the absence of bacteria.

acquire a higher diffusivity that makes them less sensitive to the action of the underlying landscape. In Fig. 4.7, we report the time evolution of the number of beads

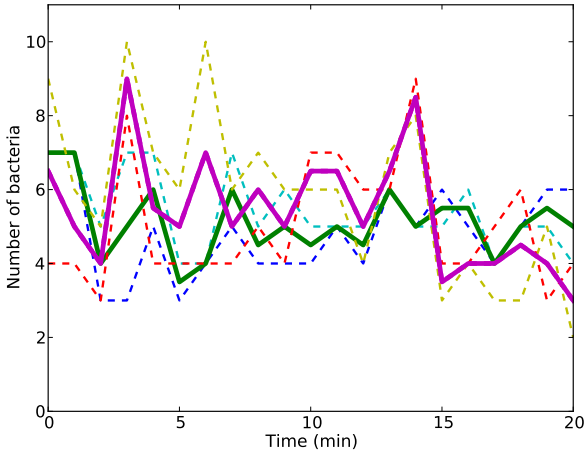

Figure 4.8: Solid lines represent the time evolution of the number of bacteria in the center of the gathering square structure (green) and in the center the scattering structure (purple). Dashed lines represent the number of bacteria in each structure.

over an entire gathering structure for the three cases $\rho_b = 0$, 0.014 and 0.2 μm^{-2}. As expected, an increased activity leads to a balancing of the two rates λ_+ and λ_- with the consequent weakening of rectification. We do not observe any appreciable accumulation effects for swimming bacteria since diffusivities, in that case, are extremely large. Moreover, the number of bacteria is not affected by the structure geometry, as shown in Fig. 4.8.

4.3.4 Structural curvature effect

A rather unexpected and significant effect is obtained changing the structures from square boundaries to circular ones (Fig. 4.9). Although both barriers have the same cross section-shaped, square structures are much more effective in gathering particles than circular ones. We hypothesize that the effect of curvature is due to the narrowing of incident angles for which a bead, driven by a constant force, is able to bypass the barriers. However, we are currently unable to exclude that the noise

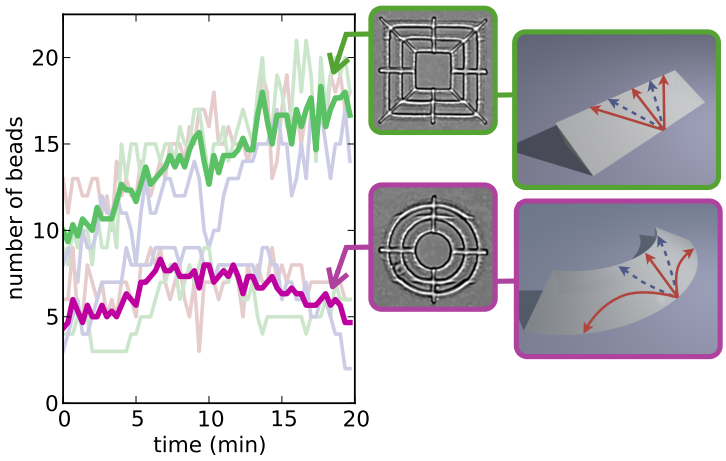

Figure 4.9: Filling efficiency for gathering structures of different curvatures. Thick solid lines represent the bead number average over three different experiments on the total area of nearby square (green) and circular (purple) structures. Unaveraged curves are color coded in the background. Additionally, we show a schematic of the effect of wall curvature on the trajectory of a particle driven by propelling force. Dotted arrows show the trajectories without gravity. In the presence of gravity the flat ramp applies a constant force while the curved ramp results in a position dependent force which is able to deflect particles more easily.

near the boundaries due to complex bacteria-particle-wall interactions contribute to this effect.

4.4 Conclusions

We have designed and implemented a novel method to use self-propelled bacteria as micro-propellers capable to transport and segregate colloids over micro-patterned structures. The proposed mechanism relies on the use of bacteria as the source of an out-of-equilibrium noise that allows colloidal particles to cross asymmetric barriers with strongly biased transition rates in opposite directions. Furthermore, in this experiment only colloidal beads are confined or dispersed. Bacteria, in fact, are free to move above structures and do not display any accumulation. This because bacteria, differently from silica beads, have a higher effective sedimentation length due

to their lower buoyancy mass and higher effective diffusion coefficient. Previously reported rectification phenomena in active matter rely on a different effect where the presence of geometric constraints drives self propelled particles along non reversible paths [6]. In contrast, here active particles are free from strict geometric constraints and rectification arises from asymmetries in the field of applied forces. As opposed to the case of 2D funnel shaped obstacles, that only provide a limited number of rectifying channels, our asymmetric 3D barriers can be crossed with biased rates at any point along their length, allowing for an increased rectification efficiency. Moreover, we use bacteria to segregate passive heavy colloidal particles, while the active bacterial component is basically unaffected by the underlying structure. It is also important to note that, since the rectification process here is driven by transitions over energy barriers that are well above k_BT, the disruptive effects of Brownian motion are significantly reduced. Further investigations on the role of barrier shape could lead to the design of optimal devices, faster and more selective which could discriminate between colloids of different size, shape or density.

Chapter 5

E.coli in holographic optical tweezers

5.1 Introduction

Optical tweezers, introduced by A.Ashkin [59], use a strongly focused laser beam to trap and move objects whose size ranges from tens of nanometers to tens of micrometers. The scattering force pushes an object such as a colloidal particle along the optical axis in the direction of propagation, while the gradient force drags it towards the focal point. The trap is stable when the gradient force prevails over the scattering force (Fig.5.1). Holographic optical tweezers can trap more objects simultaneously using a spatial light modulator (SLM). An SLM acts as a diffractive optical element splitting a single laser beam into many traps that may be independently positioned in 3D (Fig.5.2)[13]. This technique is particularly suited to the study of biological matter, like bacteria, cells and macromolecules [12, 56, 60, 61]. In fact, holographic optical tweezers can manipulate a single bacterium or more of them, thus allowing a quantitative measurement of forces involved in bacterial swimming and of the interactions between bacteria in a well-controlled and reproducible environment. Moreover, trapping bacteria with fluorescent flagella may allow us to study in detail hydrodynamic interactions and the synchronization effects between flagellar bundles and bacteria.

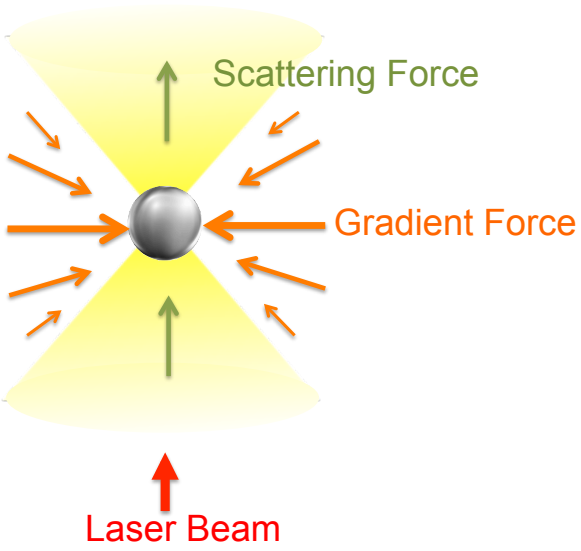

Figure 5.1: A schematic representation of forces involved in an optical trap.

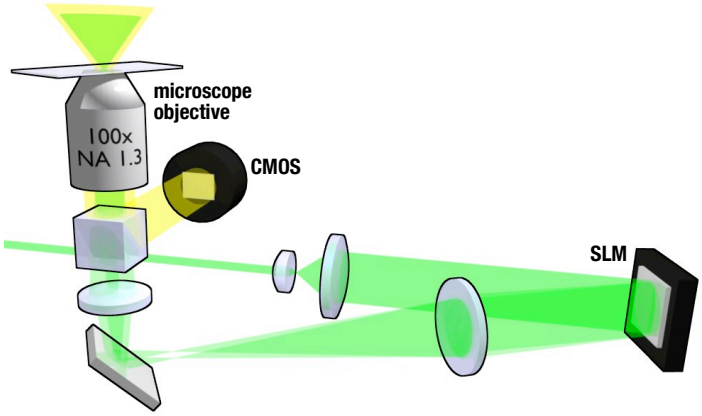

Figure 5.2: A typical setup for holographic optical trapping. A laser beam (in green) is expanded to fill the active area of the SLM. Then, the modulated beam is compressed and focused on the entrance pupil of a microscope objective with high numerical aperture. White light (in yellow) is used for imaging the trapped objects (Figure reproduced from [13]).

5.2 Photodamage

Holographic optical tweezers are a powerful tool to manipulate bacteria and other microorganisms. However, their use has some limitations, due by the potential damage on the sample resulting from trapping laser. The origin of cells photodamage in optical trapping is not fully understood. It could be due to a transient local heating, or to a two-photon absorption, or else to a photochemical process resulting in the production of reactive chemical species. The characterization of this phenomenon for *E.coli* cells has been studied across the near-infrared region favored for trapping (790-1064 nm) in [62]. Biological materials are relatively transparent to a waveband in the near-infrared region, between the absorption bands of many biological chromophores in the visible region and the increasing absorption of water toward longer wavelengths. In [62], the photodamage induced to *E.coli* cells using a bacterium attached to a cover glass by a single flagellum. The tethered cell turns around its point of attachment when flagellar motor rotates. The rotation frequency is $\sim 0 - 15$ Hz depending on the cell size. In this work the photodamage effects are quantified by the time at which rotational rate decreases of 50% compared to its initial value, LD_{50}. Bacteria trapped with an infrared laser at 1064 nm with a power of 50 mW show a decrease of 50% in rotational rate after about 15 minutes, whereas LD_{50} is 50 minutes for a free cell. Furthermore a larger increase in LD_{50} is observed by removing oxygen. Without oxygen, LD_{50} is 45 minutes. It is seen that anaerobic conditions increase the lifetime of trapped cells. Thus, the use of oxygen scavenging system is suggested to reduce oxygen in trapping experiments.

5.3 The flagella fluorescent labeling protocol

A single flagellum, described in Sec.2.2, is several micrometer long but only about 20 nm in diameter. Thus, observing a single flagellum is not straightforward. To overcome this limitation a protocol was developed in [14] to color single flagellar filament. In [14], the different polymorphic form of flagella are observed during the run-and-tumble motion using this labeling method. The fluorescent labeling method, described in [14], is applied to mark cells using Alexa Fluor (488, 532, 546, or 594) carboxylic acid succinimidyl ester or Oregon Green 514 carboxylic acid succinimidyl

ester (O-6139). The name of each dye carries a number that corresponds to the peak of its excitation spectrum (in nanometers). In [14] it is found that Alexa Fluor 532 and 594 provide the brightest dye. To label the cells, after the usual procedure to prepare *E.coli* samples (see Sec.2.3), a solution composed of 0.4 mg of Alexa Fluor dissolved in 100 μl of motility buffer, is added to bacteria sample. This compound is mixing gently at 100 rpm for 1 hour in a dark room at ambient temperature. Sodium bicarbonate (25 μm 1M) is added to solution for shift the pH to 7.8. Then, bacteria are washed three times to remove dye from the solution by centrifugation and resuspension in a motility buffer. Fig. 5.3 shows *E.coli* cells labeled with Alexa Fluor 532.

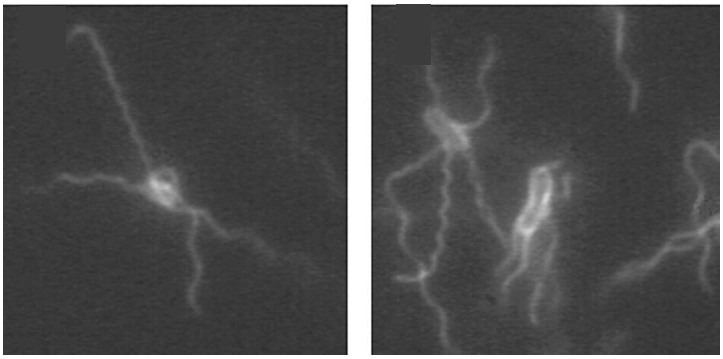

Figure 5.3: *E.coli* cells labelled with Alexa Fluor 532. Cells are illuminated by strobed argon-ion laser (Figure reproduced from [14])

5.4 Preliminary results

In the following sections, we describe our preliminary result in fluorescent labeling and trapping experiments. Our final aim is to combine these two tools to study the synchronization effects between the flagellar bundles of different cells and the hydrodynamic interactions between bacteria, through the direct observation of flagella behavior.

5.4.1 Trapping

To trap bacteria cells we use the typical setup shown in Fig.5.2 equipped with an infrared laser (Laser Quantum Ventus IR $\lambda = 1064$nm [63]), an SLM (Hamamatsu LCOS-SLM X10468 [64]) and a CMOS camera (Hamamatsu Orca Flash 2.8 [40]). The *E.coli* samples are prepared following the protocol described in Sec.2.3. In this preliminary experiments we have tested different trapping configurations to select the best setting for studing trapped bacteria. A first set of measurements is carried out using two trapping spots with a trapping power of 60 mW. The *E.coli* cell is trapped horizontally along the x-axis, as shown in Fig.5.4(a). We collect 30000 frame at 250 fps for a total time of 60 seconds. The lifetime of trapped cell is measured observing the fluctuation in the angle between the horizontal trap axis and cell axis (see Fig.5.4(b)). Since it is difficult trap a cell horizontally avoiding that the cell flips in one of the two traps, in a second set of measurement we used one trap with a trapping power of 40 mW. Thus, a bacterium is trapped along the z-axis as shown in Fig.5.5(a). In this configuration we can track the cell dynamics through the motion of its center of mass. However, this seems to produce a much larger noise-to-signal ratio. We are currently developing new strategies for 3D bacteria manipulation with holographic optical tweezers that will allow to trap a cell body along z and subsequently rotate the cell axis to lay it on the focal plane.

5.4.2 Flagella fluorescent labeling

We follow the protocol described in [14] to label fluorescent flagella. Some *E.coli* that we have labeled using Alexa Fluor 532 are shown in Fig.5.6. In a sample of labeled cells, at least 30% of cells appear to be motile. Fluorescence is observed for almost 10 minutes of constant exposure to excitation light. Our labeling protocol is still under testing. We are now trying to upgrade this protocol in order to obtain a higher fraction of motile labelled bacteria.

5.5 Future developments

We are working to improve the fluorescent labeling protocol and the trapping configuration. The next step will be to test the trapping using oxygen scavenging system

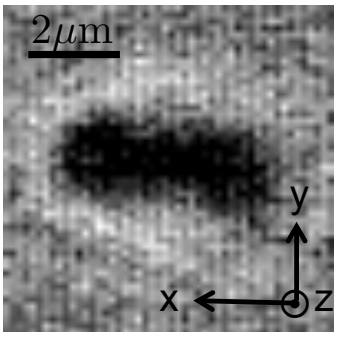

(a)

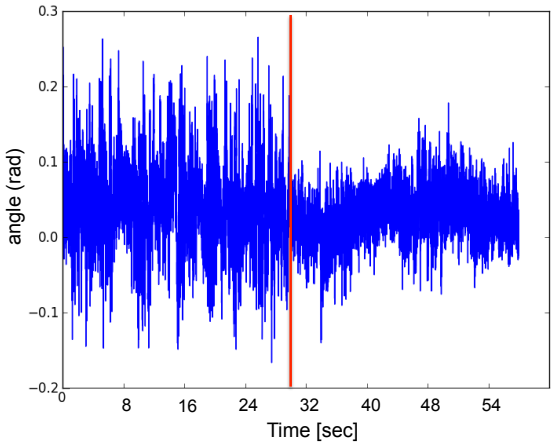

(b)

Figure 5.4: Two-trap configuration: (a) image of trapped bacterium; (b) angle between trapping axis and cell axis in time (the red bars denotes the lifetime of trapped bacteria).

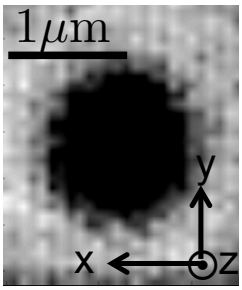

(a)

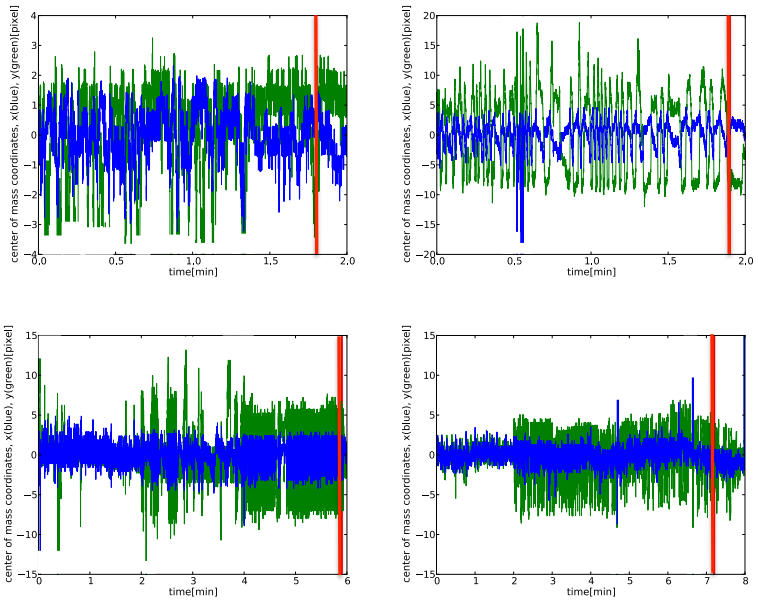

(b)

Figure 5.5: One-trap configuration: (a) the trapped *E.coli* along the z-axis; (b) centre of mass vs. time for different *E.coli* (red bars denote the lifetime of trapped bacteria).

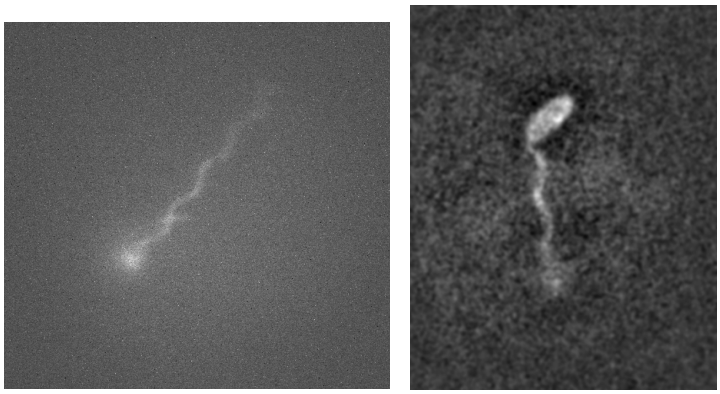

(a) (b)

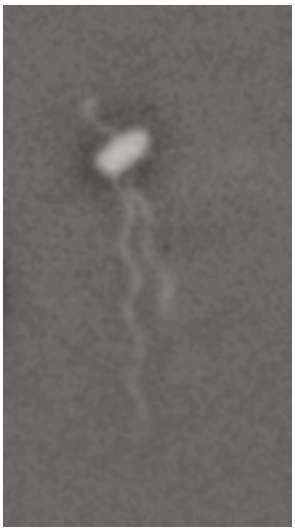

(c)

Figure 5.6: Images of fluorescent *E.coli* labelled using Alexa Fluor 532 in our laboratories. The cells are illuminated by a green LED.

to increase lifetime and develop a holographic trapping configuration to observe more bacteria simultaneously. Then, we plan to perform experiments using holographic optical tweezers to study hydrodynamics interactions between bacterial flagella.

Bibliography

[1] E.M. Purcell. Life at low Reynolds number. *American Journal of Physics*, 45(1):3–11, 1977.

[2] H.C. Berg. *E.coli in Motion*. Springer, 2004.

[3] M. E. Cates. Diffusive transport without detailed balance in motile bacteria: Does microbiology need statistical physics? *Reports on Progress in Physics*, 75(4), 2012.

[4] J. Tailleur and M. E. Cates. Sedimentation, trapping, and rectification of diluite bacteria. *Europhysics Letter*, 86(60002), 2009.

[5] J. Palacci, C. Cottin-Bizonne, C. Ybert, and L. Bocquet. Sedimentation and effective tempereture of active colloidal suspension. *Physical Review Letters*, 105(088304), 2010.

[6] P. Galajda, J. Keymer, P. Chaikin, and R. Austin. A wall of funnels concentrates swimming bacteria. *Journal of Bacteriology*, 189(23):8704–8707, 2007.

[7] R. Di Leonardo, L. Angelani, D. Dell'Arciprete, G.Ruocco, V.Iebba, S. Schippa, M.P. Conte, F. Mecarini, F. De Angelis, and E. Di Fabrizio. Bacterial ratchet motors. *Proceeding of the National Academy of Science of the United States*, 107(21):9541–9545, 2010.

[8] C. Maggi, A. Lepore, J. Solari, A. Rizzo, and R. Di Leonardo. Motility fractionation of bacteria by centrifugation. *Soft Matter*, 9(45):10885–10890, 2013.

[9] N. Koumakis, A. Lepore, C. Maggi, and R. Di Leonardo. Targeted delivery of colloids by swimming bacteria. *Nature Communication*, 4(2588), 2013.

[10] J. Adler and B.Templeton. The effect of enviromental conditions on the motility of *Escherichia coli*. *Journal of General Microbiology*, 46:175–184, 1967.

[11] M. Prummer, D. Kling, V. Trefzer, T. Enderle, S. Zoffmann, and M. Prunotto. A random motility assay based on image correlation spectroscopy. *Biophysical Journal*, 104:2362–2372, 2013.

[12] A. Ashkin and J.M. Dziedzic. Optical trapping and manipulation of viruses and bacteria. *Science*, 235, 1987.

[13] M. Padgett and R. Di Leonardo. Holographic optical tweezers and their relevance to lab on chip devices. *Lab on a Chip*, 7, 2011.

[14] L. Turner, W.S. Ryu, and H.C. Berg. Real-time imaging of fluorescent flagellar filaments. *Journal of Bacteriology*, 182, 2000.

[15] G.I. Menon. *Rheology of complex fluid*, chapter Active matter, pages 193–218. Springer, 2010.

[16] J. Adler. Chemotaxis in bacteria. *Annual Review of Biochemistry*, 44:341–356, 1975.

[17] E. Lauga and T.R. Powers. The hydrodynamics of swimming microorganisms. *Reports on Progress in Physics*, 72, 2009.

[18] E.M. Purcell. The efficiency of propulsion by a rotating flagellum. *Proceeding of the National Academy of Science of the United States*, 94:11307–11311, 1997.

[19] M. J. Schnitzer. Theory of continuum random walk and application to chemotaxis. *Physica Review E*, 48(2), 1993.

[20] J. Tailleur and M. E. Cates. Statistical mechanics of interacting run-and-tumble bacteria. *Physical Review Letters*, 100(21), 2008.

[21] J. B. Perrin. Mouvement brownien et réalité moléculaire. *Ann. Chimie et Physique*, 8:1–114, 1909.

[22] R. Di Leonardo, D. Dell'Arciprete, L. Angelani, and V. Iebba. Swimming with an image. *Physical Review Letters*, 106, 2011.

[23] M. Godin, A. K. Bryan, T. P. Burg, K. Babcock, and S. C. Manalis. Measuring the mass, density, and size of particles and cells using a suspended microchannel resonator. *Applied Physics Letters*, 91(12):123121–123123, 2007.

[24] F. R. Blattner, G. Plunkett III, C. A. Bloch, N. T. Perna, V. Burland, M. Riley, J. Collado-Vides, J. D. Glasner, C. K. Rode, G. F. Mayhew, J. Gregor, N. W. Davis, H. A. Kirkpatrick, M. A. Goeden, D. J. Rose, B. Mau, and Y. Shao. The complete genome sequence of *Escherichia coli* K-12. *Science*, 277:1453, 1997.

[25] T. Baba, T. Ara, M. Hasegawa, Y. Takai, Y. Okumura, M. Baba, K.A. Datsenko, M.Tomita, B.L. Warren, and H. Mori. Construction of *Escherichia coli* k-12 in-frame, single-gene knockout mutants: the keio collection. *Molecular System Biology*, 2, 2006.

[26] E. Lauga, W. R. Di Luzio, G.M. Whitesides, and H. A. Stone. Swimming in circles: Motion of bacteria near solid boundaries. *Biophysical Journal*, 90:400–412, 2006.

[27] A. Campbell. Synchronization of cell division. *Bacteriology Reviews*, 21(4):263–272, 1957.

[28] L. M. Maurer, E. Yohannes, S. S. Bondurant, M. Radmacher, and J. L. Slonczewski. pH regulates genes for flagellar motility, catabolism, and oxidative stress in *Escherichia coli* K-12. *Journal of Bacteriology*, 187(1):304–319, 2005.

[29] D. L. Taylor, J. S. Condeelis, P. L. Moore, and R . D . Allen. The contractile basis of amoeboid movements. *Journal of Cell Biology*, 59:378–394, 1973.

[30] J. Henrichsen. Bacterial surface translocation: a survey and a classification. *Bacteriology Reviews*, 36(4):478–503, 1972.

[31] K. M. Otterman and J. F. Miller. Roles for motility in bacteria-host interactions. *Molecular Microbiology*, 24(6):1109– 1117, 1997.

[32] J. Adler and M.M Dahl. A methot for measuring the motility of bacteria and for comparing random and non-random motility. *Journal of General Microbiology*, 46(1):161–173, 1967.

[33] H.C. Berg and D. A. Brown. Chemotaxis in *Escherichia coli* analysed by three-dimensional tracking. *Nature*, 239:500–504, 1972.

[34] H.C. Berg. How to track bacteria. *Review of Scientific Instruments*, 42(6), 1971.

[35] R. Cerbino and V. Trappe. Differential dynamic microscopy: probing wave vector dependent dynamics with a microscope. *Physical Review Letters*, 100, 2008.

[36] N. O. Petersen, P. L. Hoddelius, P. W. Wiseman, O. Serger, and K. Magnusson. Quantitation of membrane receptor distributions by image correlation spectroscopy: Concept and application. *Biophysical Journal*, 65:1135–1146, 1993.

[37] L. G. Wilson, V.A. Martinez, J. Schwarz-Linek, J. Tailleur, G.Bryant, P.N. Pusey, and W.C.K. Poon. Differential dynamic microscopy of bacteria motiliy. *Physical Review Letters*, 106, 2011.

[38] B. J. Bern and R. Pecora. *Dynamic Light Scattering*. Courier Dover Publications, 1975.

[39] V.A. Martinez A. Martinez, R. Besseling, O. A. Croze, J. Tailleur, M. Reufer, J. Schwarz-Linek, L. G. Wilson, M. A. Bees, and W. C. K. Poon. Differential dynamic microscopy: a high-throughout method for characterizing the motility of microorganism. *Biophysical Journal*, 103(8):1637–1647, 2012.

[40] http://www.hamamatsucameras.com/orca-flash/.

[41] http://www.python.org/.

[42] https://nic.med.harvard.edu/VALAP 2010.

[43] H. C. Berg and L. Turner. Selection of motile nonchemotactic mutants of escherichia coli by field-flow fractionation. *Proceding of National Academy of Science of the United States of America*, 88:8145–8148, 1991.

[44] S. Y. Kim, E. S. Lee, H. J. Lee, S. Y. Lee, S. K. Lee, and T. Kim. Microfabricated ratchet structures for concentrating and patterning motile bacterial cells. *Journal of Micromechanics and Microengineering*, 20(9), 2010.

[45] S. E. Hulme, W. R. DiLuzio, S. S. Shevkoplyas, L. Turner, M. Mayer, H. C. Bergc, and G. M. Whitesides. Using ratchets and sorters to fractionate motile cells of *Escherichia coli* by length. *Lab on a Chip*, 8:1888–1895, 2008.

[46] G. H. Seward. *Optical Design of Microscopes*. SPIE Tutorial Text, 2010.

[47] G. B. Stock. Application of splines to the calculation of bacteria swimming speed distribution. *Biophysical Journal*, 16:535–540, 1976.

[48] C. Valeriani, M. Li, J. Novosel, J. Arlt, and D. Marenduzzo. Colloids in a bacterial bath: simulations and experiments. *Soft Matter*, 7:5228–5238, 2011.

[49] L. Angelani, C. Maggi, M. L. Bernadini, A. Rizzo, and R. Di Leonardo. Effective interactions between colloidal particles suspended in a bath of swimming cells. *Physical Review Letters*, 107:138302, 2011.

[50] X. Wu and A. Libchaber. Particle diffusion in a quasi-two-dimensional bacterial bath. *Physical Review Letters*, 84:3017–3020, 2000.

[51] N. Darnton, L. Turner, K. Breuer, and H. C. Berg. Moving fluid with bacterial carpets. *Biophysical Journal*, 86:1863–1870, 2004.

[52] D. B Weibel, P. Garstecki, D. Ryan, W.R. Di Luzio, M. Mayer, J. E. Seto, and G. M. Whitesides Whitesides. Microoxen: Microorganisms to move microscale loads. *Proceding of National Academy of Science of the United States of America*, 102:11963–11967, 2005.

[53] B. Behkam and M. Sitti. Bacterial flagella-based propulsion and on/off motion control of microscale objects. *Applied Physics Letters*, 90(023902), 2007.

[54] R. Fernandes, M. Zuniga, F.R. Sassine, F. Karakoy, and D. H. Gracias. Enabling cargo-carrying bacteria via surface attachment and triggered release. *Small*, pages 588–592, 2011.

[55] E. Steager, C. B. Kim, J. Pateland S. Bith, and C. Naik. Control of microfabricated structures powered by flagellated bacteria using phototaxis. *Applied Physics Letters*, 90(263901), 2007.

[56] D. G. Grier. A revolution in optical manipulation. *Nature*, 424, 2003.

[57] R. Di Leonardo, V. Ianni, and G. Ruocco. Computer generation of optimal holograms for optical trap arrays. *Optics Express*, 15:1913–1922, 2007.

[58] S. Bianchi and R. Di Leonardo. Real-time optical micro-manipulation using optimized holograms generated on the GPU. *Computer Physics Communication*, 181:1444–1448, 2010.

[59] A. Ashkin. Acceleration and trapping of particle by radiation pressure. *Physical Review Letters*, 24(4), 1970.

[60] S. Chattopadhyay, R. Moldovan, C. Yeung, and X. L. Wu. Swimming efficiency of bacterium *Escherichia coli*. *Proceeding of the National Academy of Science of the United States*, 103(37):13712–13717, 2006.

[61] T. L. Min, P. J. Mears, L. M. Chubiz, C. V. Rao, I. Golding, and Y. R. Chemla. High-resolution, long-term characterization of bacteria motility using optical tweezers. *Nature Methods*, 6(11):831–835, 2009.

[62] K. C. Neuman, E. H. Chadd, G. F. Liou, K. Bergman, and S. M. Block. Characterization of photodamage to *Escherichia coli* in optical traps. *Biophysical Journal*, 77:2856–2863, 1999.

[63] http://www.laserquantum.com/products/detail.cfm?id=22.

[64] http://www.hamamatsu.com/jp/en/technology/innovation/lcos-slm/index.html.